THE ASTROPHYSICAL JOURNAL, 393:484–507, 1992 July 10

TRANSFORMATIONS OF GALAXIES. I. MERGERS OF EQUAL-MASS STELLAR DISKS

JOSHUA E. BARNES
Institute for Astronomy, University of Hawaii, 2680 Woodlawn Drive, Honolulu, HI 96822
Received 1991 August 8; accepted 1992 February 6

ABSTRACT

This paper presents self-consistent numerical results for a small sample of merging encounters between equal-mass disk galaxies. These calculations illustrate how self-gravitating disks respond to tidal perturbations and suggest an improved point of view on orbital decay in multicomponent systems. Preexisting spheroidal components merge rather gently, but the incomplete violent relaxation of the *disks* themselves is accompanied by a large drop in coarse-grained phase-space density. A detailed analysis of the orbital structure of these merger remnants shows how their shapes and kinematic properties are related to the initial disk spin vectors and other encounter parameters. Many of these remnants exhibit significant misalignment between their minor and rotation axes, a result which may constrain the number of elliptical galaxies formed by purely stellar-dynamical mergers.

Subject headings: galaxies: formation — galaxies: interactions — galaxies: kinematics and dynamics — methods: numerical — videotapes

Accompanying videotape: ApJ, 393, Part 1, No. 2, Videotape, Segment 2

1. INTRODUCTION

A wide range of theoretical studies have shown that violently interacting galaxies are subject to rapid orbital decay (e.g., Holmberg 1941; Alladin 1965; Toomre & Toomre 1972, hereafter TT; White 1978). As TT and later authors have emphasized, the end product of this decay is a merger of the galaxies involved. Further numerical simulations (see White 1983a; Barnes 1990a) have supported the hypothesis that mergers between typical disk galaxies produce remnants with the overall morphology and structural parameters of elliptical galaxies. But the specific role played by mergers between galaxies similar to present-epoch disks in the formation of nearly normal ellipticals is still controversial (e.g., Ostriker 1980; Schweizer 1990; Kormendy 1990), despite very general arguments indicating that significant merging must have occurred during the formation of most galaxies (e.g., Toomre 1977; White & Rees 1978; Efstathiou 1990).

Recent observational and numerical developments may provide a way out of this impasse. On the observational side, many elliptical galaxies are now known to have subtle distinguishing features which may reflect some part of their formation histories (see de Zeeuw & Franx 1991). These include "shells" of starlight most effectively detected by unsharp masking, isophotes showing disklike or boxlike departures from a perfect ellipse, and counterrotating cores or otherwise remarkable kinematics. Many of these features have been attributed to mergers of some kind (e.g., Schweizer 1982; Quinn 1984; Kormendy 1984; Binney & Petrou 1985; Nieto & Bender 1989; Balcells & Quinn 1990). On the numerical side, improved N-body algorithms (e.g., Greengard 1990) and faster hardware have greatly expanded the scope for computer simulations of galactic encounters. The experimental methodology can now support the construction of relatively definitive dissipationless models of interacting and merging disk galaxies, while models including gasdynamics are probably limited largely by our incomplete knowledge of the physics of interstellar material and our fragmentary understanding of star formation.

The work described here was motivated by the long-standing idea that a detailed analysis of remnant properties might constrain the number of elliptical galaxies produced by essentially stellar-dynamical mergers of disk galaxies. Following the approach of Barnes (1988, hereafter B88), a self-consistent N-body code was used to simulate parabolic encounters and mergers between equal-mass disk/halo galaxies. But while B88 considered only direct and retrograde versions of an encounter between two symmetrically inclined disks, the present study set out to sample coarsely but systematically the space of all possible disk orientations. In addition, these calculations were run with up to 4 times as many particles, significantly reducing the effects of two-body relaxation. The new simulations thus provide a plausible starting point for a comparative study of merger remnants. Such a study, including an analysis of the orbital structure of near-equilibrium remnants, is the main goal of this paper. In passing, however, the new models also vividly illustrated the behavior of self-gravitating disks subjected to tidal forces and provided further insight into the process of orbital decay in multicomponent systems. Moreover, the relatively large numbers of particles used in these calculations allowed more accurate measurements of remnant density profiles and maximum phase-space densities.

To present these results in an orderly fashion, the outline of this paper roughly follows the steps leading up to the orbital analysis of remnant structure. Properties of the initial galaxies are summarized in § 2.1, and parameters for a modest sample of parabolic encounters between equal-mass disk galaxies are described in § 2.2. The dynamical evolution of the encounter models is discussed in § 3, focusing on the behavior of the disks in § 3.1, the decay of the galactic orbits in § 3.2, and the ensuing mergers in § 3.3. The equilibrium structure of the merger remnants is described in § 4, covering profiles and characteristic scales in § 4.1, shapes and rotation in § 4.2, and orbital structure in § 4.3. Further remarks and conclusions are presented in § 5. Details on the initial galaxy models are given in Appendix A, and a synopsis of the accompanying videotape (ApJ, 393, Part 1, No. 2, Videotape, Segment 2) appears in Appendix B.

2. STELLAR-DYNAMICAL ENCOUNTER MODELS

Since two-body relaxation times in disk galaxies are many orders of magnitude greater than a Hubble time, the evolution of a galaxy composed only of stars and dark matter is accurately described by the *collisionless* Boltzmann equation (e.g., Binney & Tremaine 1987), coupled to Poisson's equation for the mean gravitational field. An N-body model is essentially a Monte Carlo solution of these equations (e.g., Hernquist & Barnes 1990). The fidelity of such a solution depends on the number of particles N, the force softening scale ϵ, and whatever additional parameters control the accuracy of the force calculation and orbit integration.

2.1. *Model Disk/Halo Galaxies*

The disk galaxies used in these experiments are similar to those employed in B88. Each galaxy consists of a central bulge, a rotating exponential disk, and an extended massive halo. All three components are modeled as N-body systems with thousands of particles each. The procedure used to generate initial galaxy models is described in Appendix A.

Two different galaxy models are used in these experiments. Galaxy model 1 has a bulge:disk:halo mass ratio of 1:3:16, disk scale length $\alpha^{-1} = 0.083$, scale height $z_0 = 0.005$, total mass $M = 1.25$, half-mass radius $R_{1/2} \simeq 0.25$, net binding energy $E \simeq -1.37$, and angular momentum $J \simeq 0.048$. Here and elsewhere in this paper, dimensional quantities are given in an arbitrary system of units with $G \equiv 1$. Roughly scaling galaxy model 1 to the Milky Way, the units of length, time, and mass become 40 kpc, 250 Myr, and $2.2 \times 10^{11}\ M_\odot$, respectively. Galaxy model 2 has a dark halo with twice the mass and extent of model 1, but is otherwise similar.

2.2. *Encounter Parameters*

Initial conditions for these experiments are generated by launching a pair of equilibrium galaxy models at each other along a specified orbit. A pair of finite and initially well-separated galaxies will follow an approximately Keplerian trajectory up until first passage. One parameterization of such a trajectory is in terms of the orbital eccentricity e, pericentric separation R_p, and time of pericenter t_p. Most interacting galaxies probably have highly eccentric orbits and are only now coming together for the first time (TT); thus $0 \ll e \lesssim 1$. On the other hand, a pair of galaxies in an extended distribution of dark matter could be accelerated to a mildly hyperbolic encounter ($e \gtrsim 1$). The choice of parabolic encounters ($e = 1$) is a compromise between these two possibilities.

In the coordinate system used to describe these calculations, the orbital plane coincides with the x-y plane, and the two galaxies move about each other in a clockwise direction. The origin is coincident with the center of mass, and the initial Keplerian orbit was targeted so as to place the two galaxies exactly on the y-axis at pericenter. Two angles are required to specify the orientation of each axisymmetric disk galaxy; following TT's Figure 6, the angles used are the inclination i between the spin and oribital planes and the pericentric argument ω measured in the orbital plane from the line of the nodes to the y-axis.

As noted above, one of the objectives of this study was to sample uniformly the space of disk orientations. A similar goal was attempted by Farouki & Shapiro (1982), who chose to orient the spin vectors of their galaxies along the $\pm x$-, y-, and z-axes; this gave six possible orientations for each disk, and a total of 21 distinct choices for a pair of disks. In this study a different sampling, based on the symmetry axes of a regular tetrahedron, is used. The orientation of one of the disks was selected from the following four choices for (i, ω): the direct case $(0°, -)$ and three inclined, slightly retrograde cases, $(-109°, 90°)$, $(-109°, 30°)$, and $(-109°, -30°)$. The orientation of the other disk was selected from a menu exactly antiparallel to the first, namely, the retrograde case $(180°, -)$ and three inclined, slightly direct cases, $(71°, 90°)$, $(71°, 30°)$, and $(71°, -30°)$. Of course, the orientation of the tetrahedron used to generate this scheme is arbitrary. The one adopted here was motivated primarily by the desire to include the exactly direct and retrograde cases, fixing one of the tetrahedral symmetry axes parallel to the z-axis. Given this decision, it seemed rather appealing to include the nearly polar cases with $\omega = 90°$, since these should yield rather gentle interactions as a foil to the exactly in-plane passages.

This scheme yields $4 \times 4 = 16$ distinct encounters, all asymmetric, for a given set of orbital parameters. Only four of these 16 choices have been studied, but these were selected so that all eight possible disk orientations (four direct, four retrograde) are included. The encounters used in this study are listed in Table 1. Encounters 1–4 were run to examine the outcome, as a function of disk orientations, of a relatively close ($R_p = 0.2$) passage. Encounters 5–8 reiterate this set of four collisions for a somewhat wider ($R_p = 0.4$) passage. A couple of runs were then repeated with twice as many particles ($N = 65{,}536$ instead of 32,768) to evaluate the effects of particle discreteness and to generate more photogenic illustrations. Encounter **A** is simply a scaled-up version of encounter 1; a geometrical study of these initial conditions is presented in Segment 2, section 1, of the accompanying videotape. Encounter **B**, on the other hand, was run *after* a preliminary analysis showed that the remnant produced by encounter 6 had rather unusual kinematics, as described in § 4.2. Finally, encounters 9 and 10 were run with double-mass halos to study the effects of relatively wide ($R_p =$ 0.4 and 0.8) encounters. For these two runs the same disk orientation angles as encounters 2, 6, and **B** were used, since such inclined disks do not strongly perturb the process of orbital decay.

Production calculations were run using a tree code (Barnes & Hut 1986) modified to execute efficiently on a vector-based

TABLE 1

EQUAL-MASS PARABOLIC ENCOUNTERS

Model	R_p	t_p	i_1	ω_1	i_2	ω_2	N	B:D:H
A	0.2	1.0	0	...	71	30	65,536	1:3:16
B	0.4	1.0	−109	90	71	90	65,536	1:3:16
1	0.2	1.0	0	...	71	30	32,768	1:3:16
2	0.2	1.0	−109	90	71	90	32,768	1:3:16
3	0.2	1.0	−109	−30	71	−30	32,768	1:3:16
4	0.2	1.0	−109	30	180	...	32,768	1:3:16
5	0.4	1.0	0	...	71	30	32,768	1:3:16
6	0.4	1.0	−109	90	71	90	32,768	1:3:16
7	0.4	1.0	−109	−30	71	−30	32,768	1:3:16
8	0.4	1.0	−109	30	180	...	32,768	1:3:16
9	0.4	1.5	−109	90	71	90	49,152	1:3:32
10	0.8	1.5	−109	90	71	90	49,152	1:3:32

NOTE.—R_p is the pericentric separation and t_p is the time of first passage; angles i_1, ω_1 and i_2, ω_2 are the orientations of the two disks; N is the total number of particles, and B:D:H is the bulge:disk:halo mass ratio.

supercomputer (Barnes 1990b). Force evaluations accurate to $\sim 10^{-3}$ were obtained by setting the tolerance parameter $\theta = 0.7$ and including quadrupole corrections (Hernquist 1987). With these parameters, a full force calculation for $N = 65{,}536$ particles took $\sim$70–90 s on a ETA-10 and roughly half that time on a Cray-YMP (in both cases, timings are for a single processor). The spatial resolution of the force evaluation was set by the softening parameter $\epsilon = 0.015$. Particles were advanced using a time-centered leapfrog with time step $\Delta t = 1/128$ time units. Over a typical calculation, total binding energy and angular momentum were conserved to a few times 10^{-3}.

3. INTERACTION DYNAMICS

Figure 1 and Segment 0, section 2, of the accompanying videotape depict the development of encounter **A**, projecting

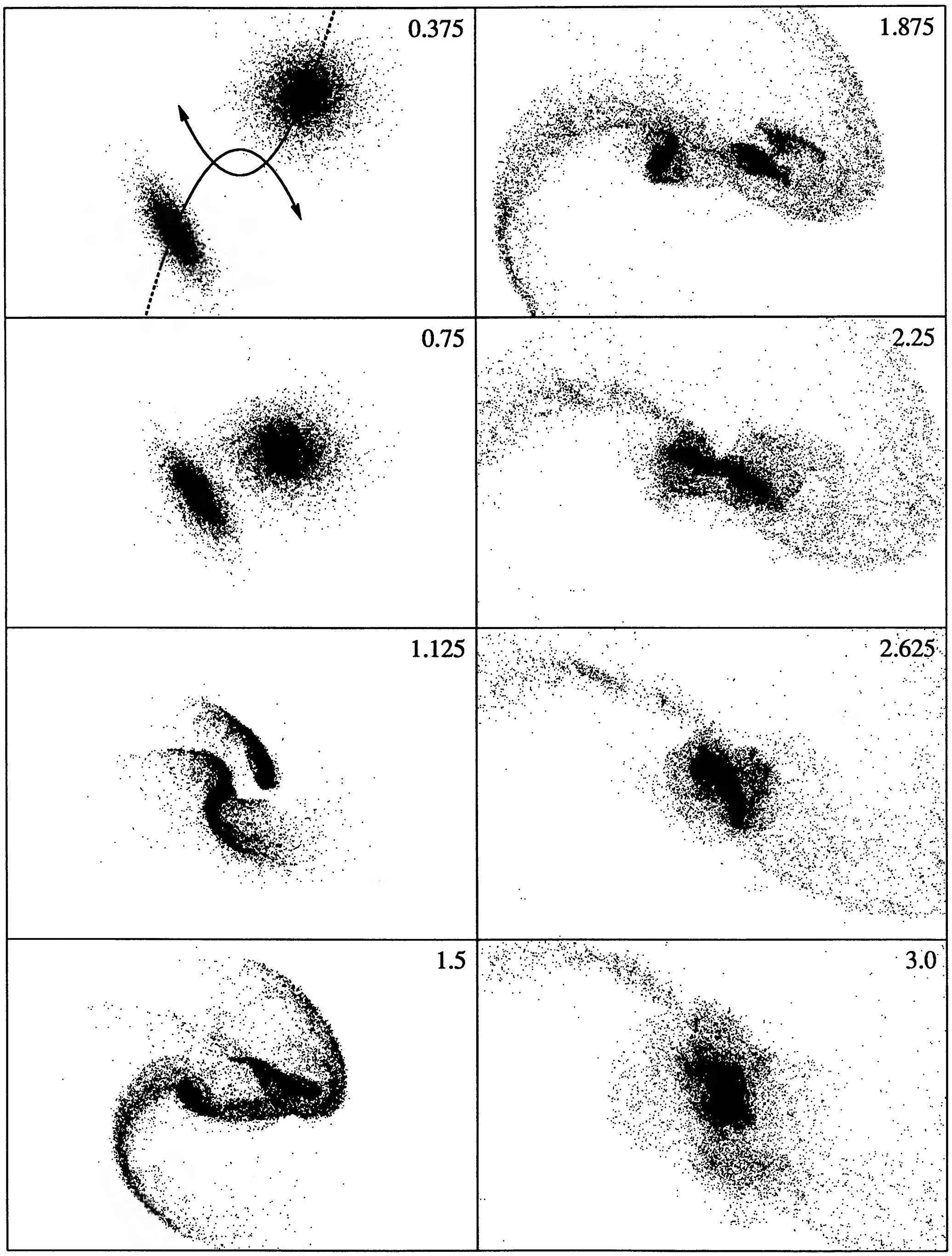

FIG. 1.—Evolution of encounter **A** projected onto the orbital plane. Only the luminous particles are plotted, with the bulge component thinned by 50% to reduce crowding. All frames are 3.6 × 2.4 length units. Times since the start are shown in the upper right-hand corners; the first frame also shows the parabolic trajectories of the incoming galaxies, drawn dashed before $t = 0$ and solid thereafter.

the luminous particles onto the orbital plane. The videos, unlike the figure, show *all* of the mass in the calculation; the halo material is shown in red, the disks in blue, and the central bulges in yellow.

The galaxies in encounter **A** interact more violently than any other pair in Table 1, essentially because of the exactly direct passage suffered by one of the disks. Indeed, this disk, seen in the upper right of the first frame, has been violently distorted into an S-shaped spiral by $t = 1.125$. The other disk in this encounter, although inclined by 71° to the orbital plane, also exhibits a strong tidal response, somewhat foreshortened from this projection. As the galaxies separate, the disks develop extended tidal tails. By this point, both galaxies have clearly departed from their initial parabolic trajectories, and by $t = 1.875$ they are already approaching each other again. They undergo a second, very close passage at $t \simeq 2.5$ and are on the point of merging at $t = 2.625$. By $t = 3.0$, the central parts of the remnant are settling into a more symmetric structure, with an elongated and roughly prolate ellipsoid embedded in a rounder distribution. At larger radii, however, this object is far from relaxed, with some material from the tidal tails still falling back toward the center, and more distant material continuing to recede toward infinity.

Segment 2, section 3, of the accompanying videotape shows encounter **A** at time $t = 1.5$, rotating the system about the vertical axis to reveal the three-dimensional structure. Note that while material from the direct disk has remained within the orbital plane, the body and tail of the inclined disk appear to define two slightly different planes. This sequence also gives a good idea of the disposition of the halo material; at the instant shown here the bulges of these galaxies are visibly displaced from the centers of their surrounding halos.

Snapshots of the other four $R_p = 0.2$ encounters at time $t = 1.5$ are shown in Figure 2. Encounter 1 is, of course, simply an $N = 32{,}768$ version of encounter **A**, and it is encouraging to note that these two models are indeed quite similar. Encounter 4, which is really a spin-reversed version of encounter 1, exhibits very different behavior. Instead of developing an extended tidal tail, the exactly retrograde disk displays an open spiral pattern and a curiously rectangular spray of material to the lower left. Its companion, nearly edge-on to the line of sight, sports a somewhat more extended tail, foreshortened from this vantage point. Encounters 2 and 3 both involve pairs of parallel but counterspinning disks. Those in encounter 3 develop respectable tidal tails, but the "bridge" linking these galaxies is an optical illusion. On the other hand, the two polar passages which make up encounter 2 have not at this stage produced impressive tails, although both disks are tidally disturbed, as are their $R_p = 0.4$ analogs to be illustrated in the next section.

3.1. *Disk Response*

The reactions of these self-gravitating galaxies to the tidal fields they experience in these simulations can be better appreciated by viewing each disk face-on. Figures 3 and 4 present such views for encounters **A** and **B**, respectively. The 12,288 disk particles of each galaxy are plotted separately. In the first view of each series, the idealized parabolic trajectory of the other galaxy is shown as a smooth curve, and in every view the actual position of the other galaxy's bulge is plotted as a small filled circle. (The curves do not *exactly* bisect the circles, as a result of the halo-driven fluctuations discussed in § 3.2.) An animated version of Figure 3 is presented in Segment 2, sections 4 and 5, of the accompanying videotape; these use the same color scheme as in the previous sequences, but mark the position of the other galaxy with a circle.

Most straightforward to describe is the exactly direct passage shown as the left-hand series in Figure 3 and in section

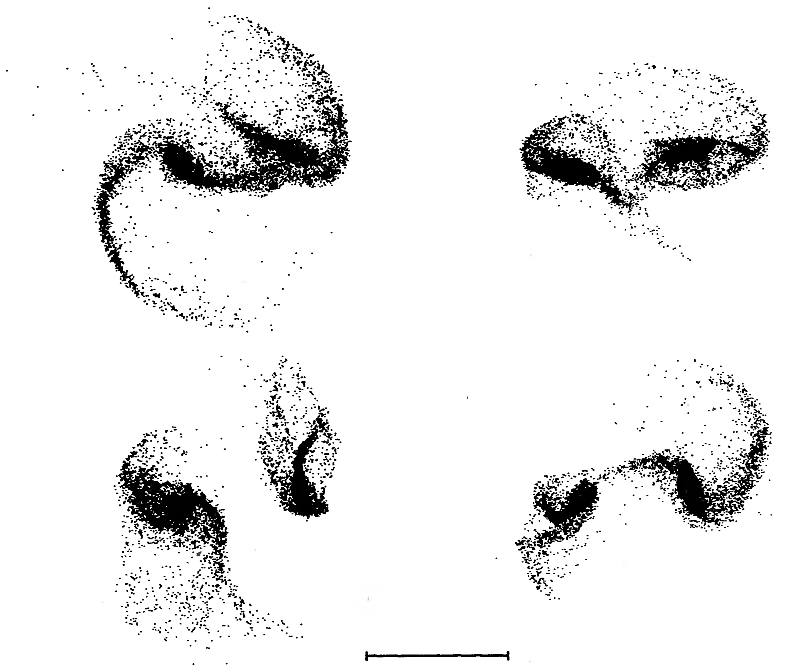

FIG. 2.—(*Clockwise from upper left*) Encounters 1, 2, 3, and 4 at time $t = 1.5$, viewed from the same vantage point as in Fig. 1. Here and after, the scale bar at the bottom is 1 unit long. Note the good agreement between encounter 1 and the corresponding frame of Fig. 1. The view of encounter 4 has been rotated by 180° so as to place the exactly in-plane disk to the left of the origin for easy comparison with the view of encounter 1.

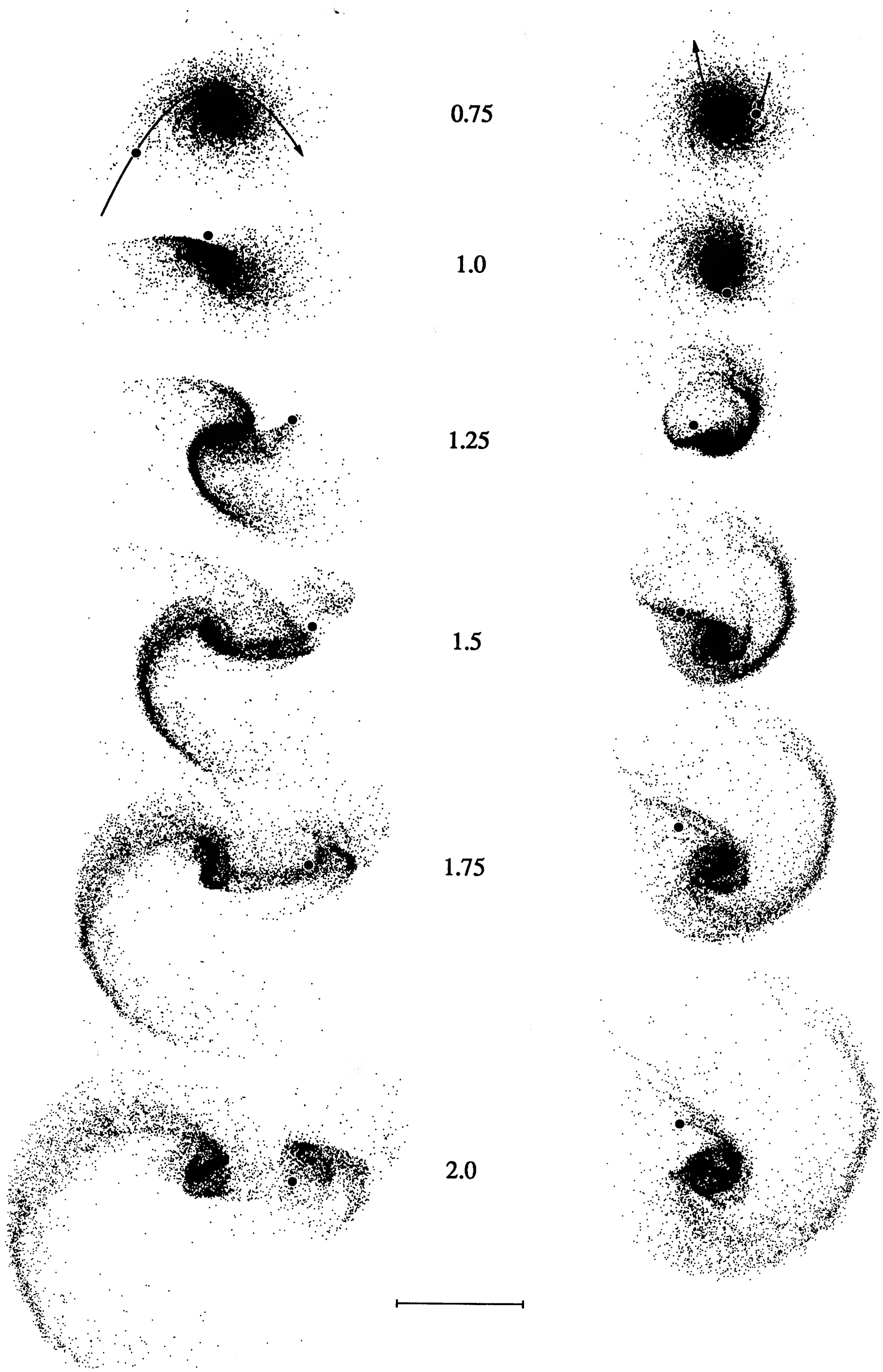

FIG. 3.—Face-on views of each of the two disks in encounter A at equally spaced times between $t = 0.75$ and 2.0. Only the 12,288 particles in each disk are plotted. The left-hand series shows the direct disk ($i = 0$), while the right-hand series shows the inclined disk ($i = 71°$, $\omega = 30°$). The first view of each series shows the initial trajectory of the other galaxy, while the filled circles show the actual position of the other bulge at each time.

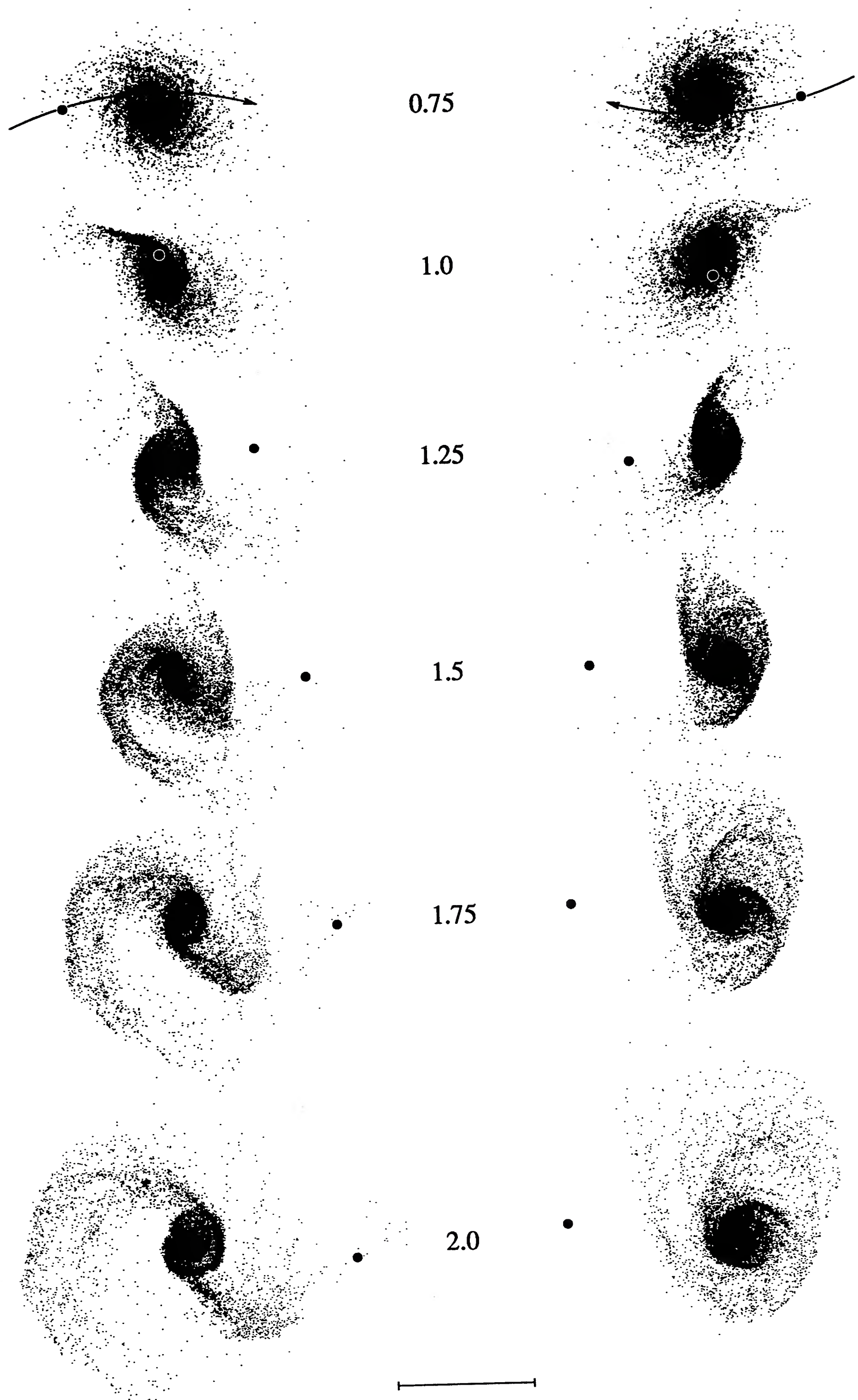

FIG. 4.—Face-on views of each of the two disks in encounter **B**. The left-hand series shows the mildly direct disk ($i = 71°$, $\omega = 90°$), while the right-hand series shows the equally retrograde disk ($i = -109°$, $\omega = 90°$). Other details are as for Fig. 2.

4 of the videotape segment. The strong tidal field present here provokes a dramatic response; even before pericenter at $t = 1.0$, the near side of the disk has already developed a sharp-edged feature which trails just behind the interloper. This feature becomes a true bridge which links the two galaxies by $t \simeq 1.5$, complete with an almost linear spur extending to the upper left of the companion. By $t = 2$, shown in the last view, a considerable amount of disk material has flowed along this bridge, piling up in a shell-like structure just to the right of the other galaxy. More striking than the bridge, however, is the massive tidal tail which develops from material on the far side of the disk at pericenter. This tail is already quite well defined at $t = 1.25$ and expands almost kinematically in subsequent views. Though quite broad when viewed face-on, it is actually extremely thin, lying as it does precisely in the orbital plane. A final signature of the strong tidal perturbation suffered by this disk is the rather massive and ponderous bar which forms at its center.

The other disk from encounter **A**, on the right in Figure 3, shows little sign of tidal damage until shortly after pericenter. By $t = 1.25$, however, it too exhibits a strong tidally generated response within a remarkably circular outline; evidently the plunging passage of its companion has produced some of the features of a ring galaxy (Lynds & Toomre 1976). Section 5 of the videotape segment illustrates the complex interplay between rotation and ring-making which places the expanding ring *above* the center of the target, despite the fact that the interloper penetrated the disk *below*. The induced ring morphology is short-lived, the far side of the ring soon opening up into an extended tidal tail, much as in some of the off-center collisions presented by Toomre (1978). The corresponding bridge is rather weak, and lying roughly in the spin plane of this disk, it does not actually connect to the other galaxy. This disk too forms a bar, although not quite as long and sluggishly turning as its companion's bar. In the last view ($t = 2$), the bar has apparently developed an inner ring, from which the outer tidal features extend.

Figure 4, derived from encounter **B**, illustrates some less dramatic reactions, due only in part to the increased pericentric distance. These two passages shown here are actually rather similar, since both disks initially lie in the same plane but spin in opposite directions; thus one encounter is slightly direct (by 19°), while the other is slightly retrograde (by the same 19°), and in both cases the pericenters are aimed as close as possible to the spin poles. And indeed, up through time $t = 1.25$ shown in the third pair of views, they have rather similar tidal features. At later times, however, the difference between direct and retrograde becomes much more obvious. The slightly direct disk develops a broad tidal tail and a fairly substantial bridge, which, however, does not effectively connect with the other galaxy. It also develops an **S**-shaped central bar, embedded in a sharply delineated disk of rather high surface density. Its retrograde counterpart exhibits a broad fan of tidal debris but no recognizable bridges or tails, nor does it develop a bar. The most striking feature of the latter disk is the two-armed "grand-design" spiral it develops at later times in response to the imposed tidal perturbation, much as seen in several other self-consistent studies of tidally disturbed disks (Toomre 1981; Hernquist 1990). Figure 5 compares a view of this disk—sampling 50% of the particles—with the analogous disk from encounter 6 at $t = 2.0$. As in the self-consistent studies of M51 presented by Hernquist (1990), the grand-design spiral evident in these views is clearly of tidal origin. The

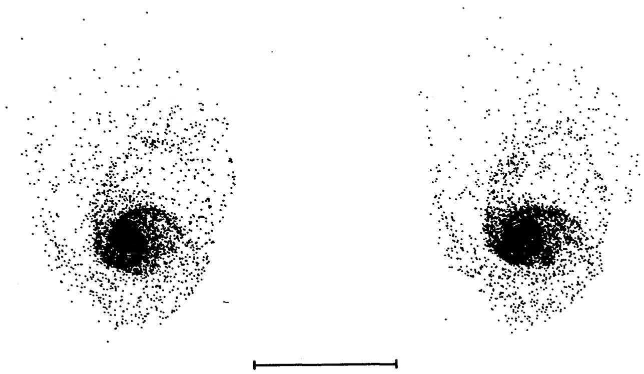

FIG. 5.—Face-on views of the corresponding retrograde disks in (*left*) encounter **B** and (*right*) encounter 6 at time $t = 2$. Only 50% of the disk particles in encounter **B** have been plotted, in order to make the visible particle density the same in both.

impression of crisper spiral structure in the left-hand frame can presumably be attributed to the smoother gravitational field of model **B**.

3.2. *Orbital Decay*

Like *every* previous self-consistent study of interactions between galaxies, the experiments presented here show that close galactic encounters are extremely "sticky," promoting rapid orbital decay. Consider the orbital trajectories plotted in Figure 4, derived by computing the bulge centroids at intervals of 0.125 time units. In every case, the incoming galaxies abandon their original parabolic trajectories shortly after first pericenter, and all eventually fall back together for even closer passages.

The four experiments used in Figure 6 have in common the initial orientations of their disks, and differ only in their target-

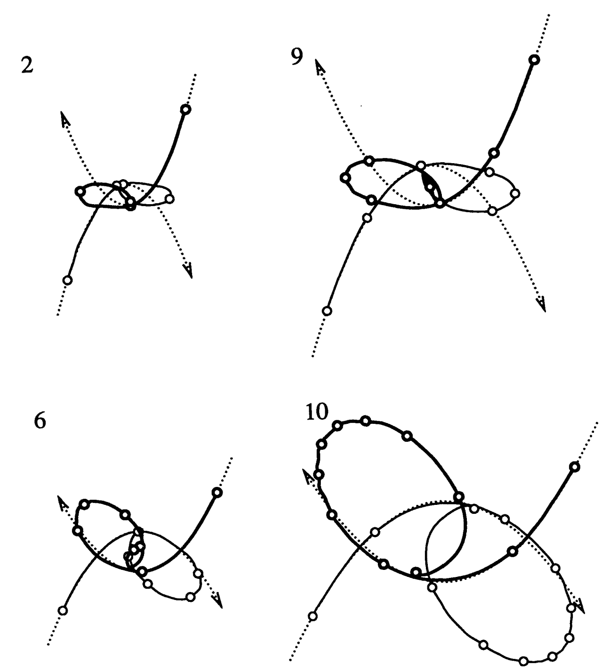

FIG. 6.—Orbital trajectories of galaxies in four encounters with identical disk orientations, but different values of R_p and halo extent. Dotted lines are the incoming parabolic orbits; solid lines show the actual paths, with open circles marking positions at unit times.

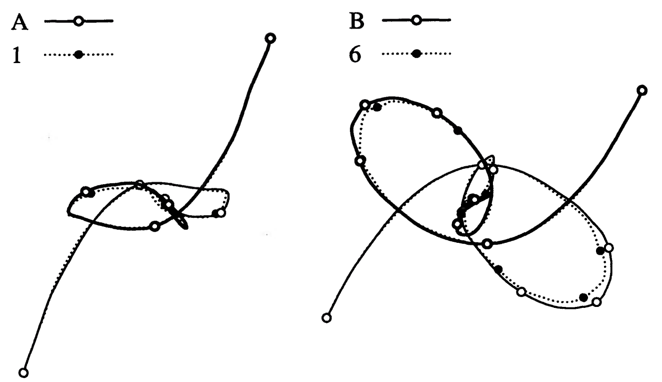

FIG. 7.—Orbital trajectories of encounters 1 and **A** and encounters 6 and **B**. Dotted lines and filled circles are used for the $N = 32{,}768$ versions, while solid lines and open circles are used for their N-65,536 counterparts.

ed pericentric separation R_p and the extent of the halos involved. From these and other examples, it appears that the shape of the actual orbits is controlled largely by the ratio of R_p to the galactic half-mass radius $R_{1/2}$; for the upper pair of encounters $R_p/R_{1/2} \simeq 0.8$, while the lower pair $R_p/R_{1/2} \simeq 1.6$. In the former case, the two galaxies interpenetrate deeply, and the attraction between them is not strong enough to hold them to their original parabolic paths. In the latter case, mutual attraction suffices to keep the galaxies on or near their initial tracks until tidal friction has robbed their relative orbit of significant angular momentum. B88 described these two cases as different modes of orbital decay. The present experiments indicate that the same dynamical mechanism is responsible for orbital decay in both cases; if so, my earlier talk of distinct "modes" was specious. Indeed, the suggestion that orbital shape is essentially a function of $R_p/R_{1/2}$ had already been advanced by Farouki & Shapiro (1982).

Orbital trajectories of several additional models are compared in Figure 7. On the left are plotted encounters 1 and **A**, the former with dotted lines and filled circles, the latter with solid lines and open circles. Although similar in overall form to the other $R_p = 0.2$ orbits just discussed, this pair of trajectories is slightly asymmetric, with the two galaxies finally meeting at a point somewhat to the right of the origin. This displacement, of course, is simply the reaction to the extended tidal tail this system ejects to the left. On the right are plotted encounters 6 and **B**. A small discrepancy between these two supposedly identical encounters is evident; the small-N version follows a somewhat tighter orbit after first passage and returns for a second encounter $\sim 5\%$ faster than its counterpart does. Such discrepancies, and the slight wiggles visible in many of these trajectories, may be due to nothing more than particle discreteness as discussed shortly.

Further insight into the orbital decay process may be obtained by examining the total angular momentum content of the two bulges, $\boldsymbol{J}_b$, computed with respect to their mutal center of mass. Figure 8 shows the z-component of $\boldsymbol{J}_b$ plotted as a function of time for all 10 numbered experiments. The top panel shows results for the $R_p = 0.2$ encounters, while the middle panel shows the $R_p = 0.4$ cases; the four runs plotted in each of these panels differ only in the initial orientations of the disks. A comparison of the various curves indicates that a change of disk orientation can alter the time between first pericenter and final merger by $\sim 20\%$ in either direction. As

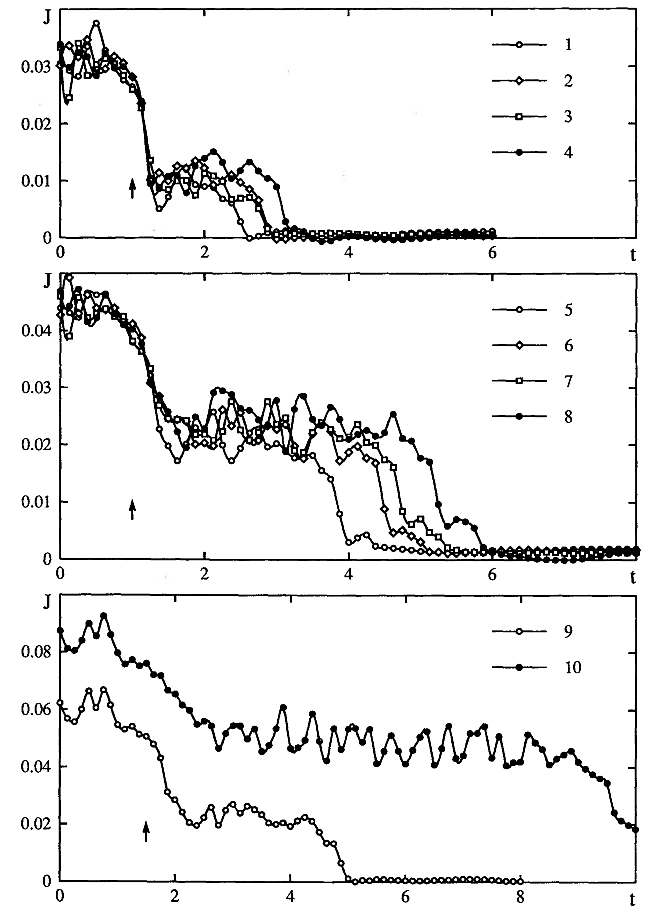

FIG. 8.—The z-component of the net angular momenta of the bulge particles in all 10 numbered encounters, plotted as a function of time. The top panel shows the $R_p = 0.2$ models, the middle panel shows the $R_p = 0.4$ encounters, and the bottom panel shows the encounters with extended halos (note that both the horizontal and vertical scales have changed). Arrows indicate first pericenter for each set of experiments.

first noted by White (1979), direct encounters decay faster than retrograde ones, suggesting that the linear transfer of spin to orbital angular momentum discussed by TT (n. 9 of their paper) and by Palmer & Papaloizou (1982) is swamped by the highly nonlinear disk response produced in these rather close encounters.

In every case, the pattern seen in Figure 8 is the same; as already noted by B88, the net angular momentum content of the bulge material drops precipitously after each passage. The final spin angular momentum of the merged bulges is in general no more than a few percent of their initial orbital angular momentum. Where does this angular momentum go? *Not* to numerical error; in these calculations, total angular momentum is conserved to one part in 10^3 or better, and numerical tests with different time steps, force-calculation parameters, and particle number yield similar orbital decay rates. To address this question, the net gravitational torques exerted on the bulge particles were measured and plotted as functions of time. The results were, at first, confusing: as one might anticipate by mentally differentiating the curves in Figure 8, the computed torques fluctuate erratically on time-scales of ~ 0.2 time units. To be sure, strong negative torques were measured just after each passage, and the time-integrated torques account for the overall decline in J_b shown in Figure 8, but this merely indicates that the numerical integration of particle trajectories was performed correctly.

The next step was to measure the partial torques exerted on the bulges by other components of the system considered individually. The results were, initially, surprising: even at the moment of deepest interpenetration, there is no significant transfer of orbital angular momentum from the bulge of one galaxy directly to the halo of the other galaxy. Instead, the force extented on a given bulge by the opposing galaxy is almost exactly along the line connecting the two at all times. As these measurements showed, the torques responsible for both the long-term evolution *and* the rapid fluctuations of J_b are essentially due to the interaction between each bulge and its *own* surrounding halo.

These results suggest the following picture of orbital decay. Initially, two massive and nonrotating halos approach each other, all angular momentum contained in their orbital motion. As the halos interact, tidal foces transfer some of this angular momentum to internal degrees of freedom; in other words, the halos start to spin. The compact central bulges, on the other hand, feel no significant tidal forces at this stage and continue with their full complement of orbital angular momentum. Shortly thereafter, the halos begin lagging behind their respective bulges, as one can see directly in the video sequences. Strong gravitational forces pull the bulges back toward the centers of the halos; these forces oppose the orbital motion of the bulges and rob them of orbital angular momentum *without imparting spin.* In a short while, the bulges are brought back into phase with their halos, and systematic transfer of angular momentum ceases. However, as a result of acquiring spin, the halos no longer have enough orbital angular momentum to maintain their original parabolic orbit. At a later date, therefore, the entire process of encounter, halo spin-up, and bulge retardation is repeated until the galaxies finally merge.

The rapid fluctuations in J_b deserve some comment. These reflect spontaneous transfers of linear momentum between each bulge and its surrounding halo. As already noted, bulges and halos are not forced to be concentric; even when no external disturbances are present, the former wanders over the relatively flat bottom of the potential well provided by the latter. The extent of these wanderings is indicated directly by the slightly wavy bulge trajectories already noted. Particularly near apocenter when the average relative velocity is small, modest perturbations in bulge momentum can translate into the $\sim 10\%$ fluctuations in J_b seen in Figure 8. The jittery behavior of these models originates in the finite sampling of phase space involved in constructing any N-body model. In the present generation of galaxy models the halo appears to be the largest source of jitter, although it may be compounded by the swing amplifier lurking in the disk.

3.3. *Final Passages*

The ultimate outcome of a series of increasingly close passages between galaxies is their merger. Figure 9 shows the last moments of the two disk galaxies in encounter **B**, which happened to conclude in a particularly attractive manner. These galaxies meet each other for the second time at $t \simeq 4.5$ and just barely survive their third passage between $t = 5.125$ and 5.25; only one object is visible in later frames. With each passage, tidal fields strip material from the disks of the two galaxies, generating various tails and other such appendages. The central bulges, more compactly built, show less damage; by definition, they are only disrupted when the two galaxies have finally merged.

The violent churning evident in the final stages of such encounters would seem an ideal setting for violent relaxation (Lynden-Bell 1967) to redistribute binding energy. Figure 10 shows how specific binding energy $E_i \equiv \phi(\boldsymbol{x}_i) + 0.5v_i^2$ of each particle i has been reappointed in encounter **B** between $t = 4.25$ and 5.5. This plot illustrates *incomplete* violent relaxation; although considerable redistribution has taken place, there is still a significant correlation between $E_i(4.25)$ and $E_i(5.5)$. Indeed, a near-perfect correlation exists for those loosely bound particles, many ejected during the first passage at $t = 1$, which were already far away when the merger took place. The remnant has a noticably deeper potential well than its precursors, but the bottom of this potential well is populated by the same components which populated the cores of the original galaxies—the bulges and the inner parts of the disks. Likewise, the broad surge of particles above the $E_i(4.5) = E_i(5.5)$ line originated in the outskirts of the victims. Thus, although binding energy has been redistributed, the outcome is reminiscent of certain schools of economic policy—the rich get richer and the poor get ejected from the system.

In many of the calculations presented here, the final collision of the two bulges seems remarkably near head-on. This may be understood as a consequence of the orbital decay mechanism described above, which removes orbital angular momentum somewhat *after* each pericenter and so does not effectively circularize the relative orbit. Of course, the bulges used in these calculations have embarrassingly large core radii, $r_c \sim 0.02$ length units, and thus present rather easy targets. Bulges with substantially smaller core radii may continue their dance for several more turns, albeit at an ever-increasing tempo, before their cores finally fuse. Incomplete violent relaxation will only partly erase detailed correlations—for example, between binding energy and metallicity (Larson 1974; Franx & Illingworth 1990)—which may be present in the victim galaxies. Thus merger remnants may inherit some of the structural properties of their progenitors. As will be shown in the next section, they also stand to inherit certain kinematic characteristics.

4. REMNANT STRUCTURE

Figure 11 portrays the continued development of remnant **A**, taking up where Figure 1 left off. On the left, tidal tails have stretched to a radius $r \simeq 8.4$ by time $t = 6$. Over much of their length these tails are freely expanding. The tip of the longer tail moves outward with a velocity of $v \simeq 1.4$; thus 5 time units after first passage, the ratio $r/v \simeq 6$ is but a slight overestimate of the time since these tails were launched. Ultimately only $\sim 6\%$ of the remnant's mass and $\sim 3\%$ of its luminosity escape to infinity. Within the escape radius $r_e(t = 6) \simeq 6.0$ the tails are bound, and within the turnaround radius $r_t(t = 6) \simeq 3.0$, material from the tails is pouring back onto the merger remnant as shown in Segment 2, section 6 of the accompanying videotape. This material, reentering in two fairly organized streams, produces a variety of shell-like features surrounding the relaxed central regions. Such structures are also seen in well-studied merger remnants such as NGC 7252 (Schweizer 1982), which likewise possesses a fine pair of tidal tails. At later times the reentry rate should decline as $t^{-5/3}$, where t is time since merger, as expected for a flat distribution of binding energies (TT).

On smaller scales this merger remnant has a much more regular appearance. In the first right-hand frame, just after merger, the remnant contains a prolate triaxial bar with a length of ~ 0.3 and an irregular, unrelaxed envelope. Phase mixing rapidly smooths out the irregularities, but the central bar persists with little change for many dynamical times.

Some idea of the three-dimensional form of this object can be had from Segment 2, sections 7 and 8, of the accompanying videotape, which present rotating views of remnant **A** at $t = 3$ and $t = 6$, respectively. The earlier view clearly shows the structures created by the infalling tails and other plumes of disk material resulting from the just-accomplished merger. In the later view such conspicuous signs are lacking. At lower "light levels," however, the remnant still exhibits a somewhat irregular outline and a hint, from some angles, of boxy or even X-shaped morphology (Binney & Petrou 1985).

The appearance of a few other merger remnants at time $t = 6$ is shown in Figure 12, a companion to Figure 2 above. Remnant 1 closely matches the appearance of the $t = 6$ large-scale view of remnant **A**; note in particular the matching shell-

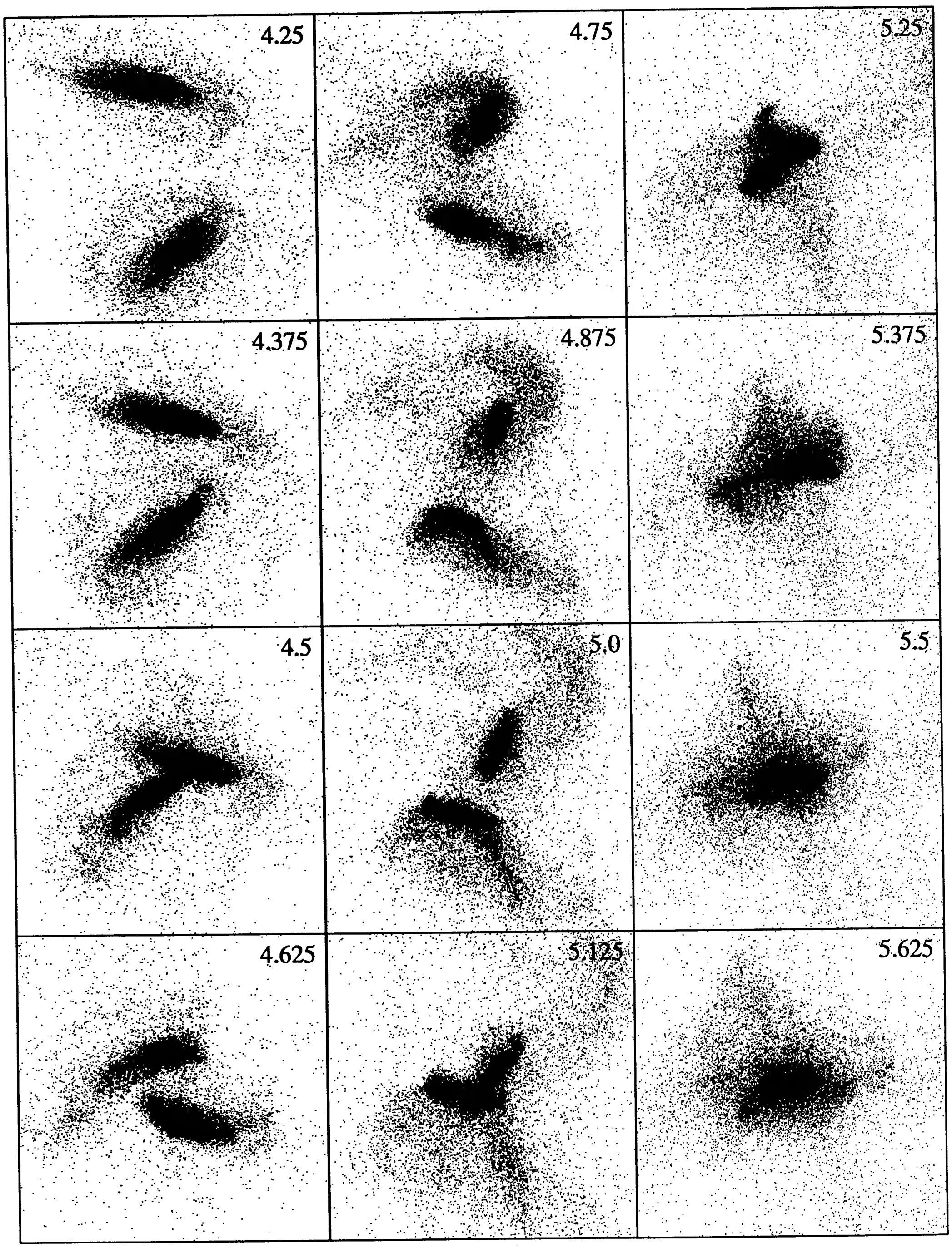

FIG. 9.—Final passages and merger of the galaxies in encounter **B**, projected onto the orbital plane. All frames are 1.2 × 1.2 length units. As in Fig. 1, only 50% of the bulge particles are plotted.

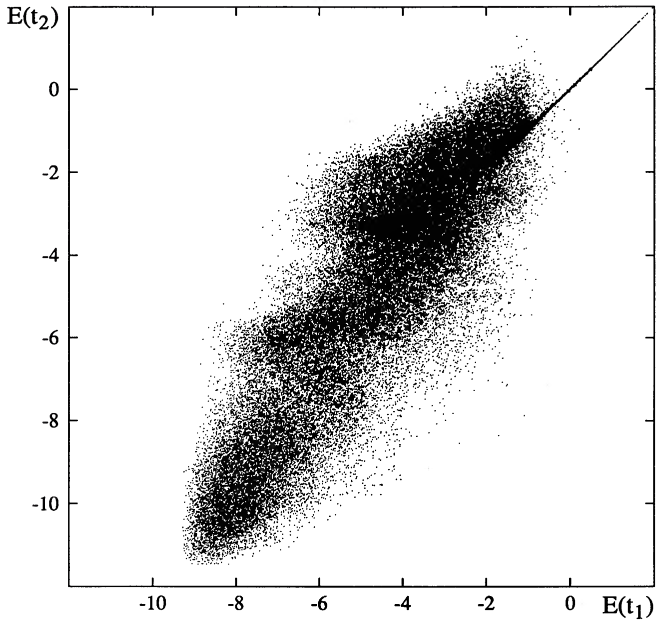

FIG. 10.—Specific binding energies of all particles in encounter **B**, compared at times $t_1 = 4.25$ and $t_2 = 5.5$.

like structures and the similar clumping of the leftmost tail in both views. Such features are apparent in some of the other remnants shown here, but not all sport a pair of well-developed tidal tails, despite their double-disk origins. In some observational circumstances the tidal appendages surrounding remnants 2 and 4 might be quite difficult to detect, and these objects might not be recognized as disk-disk mergers.

4.1. *Profiles and Characteristic Scales*

Although merger remnants are generally somewhat flattened, it is instructive to derive remnant density profiles by spherical averaging. Figure 13 shows density profiles $\rho(r)$ for remnant **B**, which are typical of the standard-galaxy mergers described here. These profiles were calculated by binning particles in finely sampled, logarithmically spaced shells and then combining adjacent shells to obtain consistently accurate densities throughout the range measured. To further reduce noise, five snapshots of the remnant between times $t = 9$ and 10 were registered and superposed; such processing effectively averages over the orbital phases of individual particles. In Figure 13 the heavy solid line shows the total mass density, the lighter solid line shows the density of luminous matter, and the dotted lines are derived from particles originating in the bulge, disk, and halo of the initial galaxies.

No single power law describes the density profiles of this object, although the total mass density appears to have a logarithmic slope of ~ -2 in the range $-1.5 \lesssim \log r \lesssim -0.5$, and a steeper slope, perhaps -4, at larger radii. The latter slope is of course predicted from a simple phase-mixing argument (e.g., White 1987; Jaffe 1987), and the transition from the shallower slope occurs at a radius containing $\sim 60\%$ of the total mass, which seems not unreasonable. The "bumps" beyond $\log r \simeq 0$ may simply reflect incomplete phase mixing.

The luminous material follows a similar pattern at large radii but exhibits a steeper slope, perhaps -3, at intermediate r. Within the core the luminous material contributes more than 90% of the mass, but this falls to 50% at $r \simeq 0.08$ and to only $\sim 10\%$ at $r = 1$; thus luminosity and mass are still significantly segregated. As might be expected from the discussion of Figure 10, the bulge dominates at small radii, but the disk makes a surprisingly large contribution, $\sim 40\%$ or more, right to the innermost point measured.

Core radii may be estimated directly from the data plotted in Figure 13 using the relation $\rho(r_c) = 2^{-3/2}\rho(0)$ appropriate for a modified Hubble law (Rood et al. 1972). The mass, light, and bulge distributions all yield nearly identical core radii; values for the disk and halo populations are uncertain, since their density profiles continue to rise through the innermost point. Consistent results are obtained by estimating core radii from the relation $r'_c = [9\sigma^2/4\pi G\rho(0)]^{1/2}$, where σ is the central one-dimensional rms velocity dispersion, appropriate for an isothermal sphere (e.g., Binney & Tremaine 1987). Although core velocity dispersion tensors are generally anisotropic, the good agreement of these two estimators provides some justification for using the isotropic isothermal sphere to estimate maximum phase-space densities from $f_{\max} = \rho(0)/(2\pi\sigma^2)^{3/2}$. Results for various components of remnant **B** and for the bulge of an initial disk model are listed in Table 2.

These measurements bring up several points. First, the core radii of the initial bulges are comparable to the radii derived for the various self-gravitating components of the remnant; evidently the former more or less determines what the latter will turn out to be. These core radii are, of course, dangerously close to the softening length $\epsilon = 0.015$ used in these experiments, but while softening perturbs the solution of Poisson's equation, it does not in itself compromise an N-body solution of the collisionless Boltzmann equation. In other words, test particles following the initial galaxies *could* evolve in the potential of a carefully choreographed mass distribution so as to produce the core radii obtained here. Note that while collisional relaxation may have modified the detailed structure of the core, evolution is probably precluded by the large softening employed and the ~ 2000 particles within the core at any instant.

Second, the coarse-grained maximum phase-space density $f_{\max}$ of the bulge material declined by only $\sim 30\%$ from start to finish. The actual decline may be even smaller, since these estimates neglect the velocity anisotropy of the final state. This rather modest change in $f_{\max}$ seems to suggest that the final coalescence of the bulge cores was rather gentle, mixing relatively little vacuum with the phase fluid.

Third, material from the disks accounts for nearly 25% of the maximum remnant phase-space density of the luminous

TABLE 2

CORE PARAMETERS FOR VARIOUS COMPONENTS OF REMNANT **B** AND FOR THE BULGE OF AN INITIAL DISK GALAXY

Component	σ^2	$\rho(0)$	r_c	r'_c	$f_{\max}$
Remnant mass	0.93 ± 0.04	1850 ± 200	0.021 ± 0.002	0.019	130
Remnant light	0.84 ± 0.04	1600 ± 200	0.021 ± 0.001	0.019	130
Remnant bulge	0.75 ± 0.03	1000 ± 100	0.021 ± 0.001	0.023	100
Initial bulge	0.38 ± 0.02	550 ± 100	0.025 ± 0.002	0.022	150

NOTE.—Central velocity dispersions, densities, core radii, and maximum phase-space densities for the remnant produced by encounter **B** and for the bulge of an initial disk galaxy. The quoted errors were estimated by comparing five measurements made between $t = 9$ and 10; systematic errors may be larger.

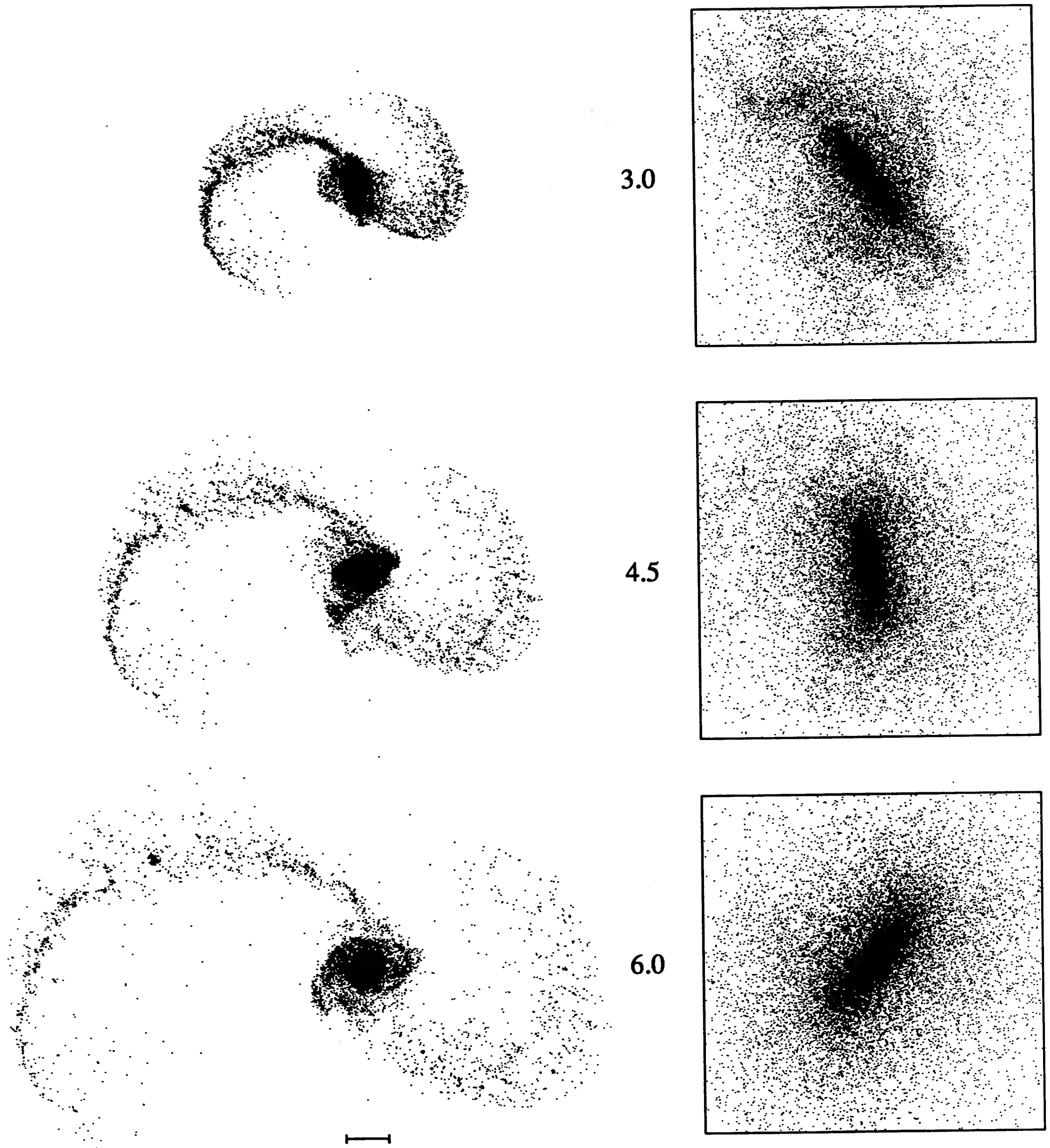

FIG. 11.—Large-scale (*left*) and small-scale (*right*) structure of the merger remnant in encounter **A**, projected onto the orbital plane, at times 3, 4.5, and 6. The boxes, enlarged by a factor of 10 from their unframed counterparts, are 0.8 × 0.8 length units. Again, only 50% of the bulge particles are plotted.

material. This result becomes somewhat less surprising in view of the relatively high initial phase-space density in the disk; normalizing the integral of the disk distribution function (eq. [A2]) to $M_d = 0.1875$, the space density and the peak phase-space density at the center of the disk are $\rho_d \simeq 430$ and $f_{\max,d} \simeq 300$, respectively. The latter actually increases with r in this constant–scale-height disk model (eq. [A3]), but inasmuch as most of the disk material in the core of the remnant came from radii within $\sim\alpha^{-1}$ initially, the central $f_{\max,d}$ is probably the relevant number to consider (e.g., Carlberg 1987). In actual simulations this $f_{\max,d}$ value is eroded due to disk heating by transient fluctuations (e.g., Carlberg & Sellwood 1985). Test runs following the evolution of a single-disk galaxy model like those used in encounter **A** show the random velocities of disk particles increasing by $\sim$30% over four rotation periods, corresponding to a roughly twofold reduction in the coarse-grained phase-space density. Even allowing for this heating, however, the final $f_{\max,d}$ in the remnant is $\sim$5 times smaller than it would have been if the merger had not taken place. Such large changes in the coarse-grained phase-space density are presumably inevitable when the cold disks of the original galaxies are violently scrambled to produce a hot remnant.

Turning from the core to larger structures, it is worth noting that the overall scale of this remnant can be quite accurately predicted by a simple energy conservation argument (Hausman & Ostriker 1978; White 1983a). Neglecting material escaping to infinity, the remnant produced by a parabolic encounter of two identical galaxies has a mass M and binding energy $E = T + U$ just twice that of its individual progenitors. Invoking the virial theorem both before and after merger, the remnant's mean one-dimensional velocity dispersion $\sigma_m^2 \equiv \frac{2}{3}T/M$ should be identical to that of the victims, while the gravitational radius $r_g \equiv GM^2/|U|$ (Binney & Tremaine 1987) should be just twice that of the initial galaxies. For a remnant

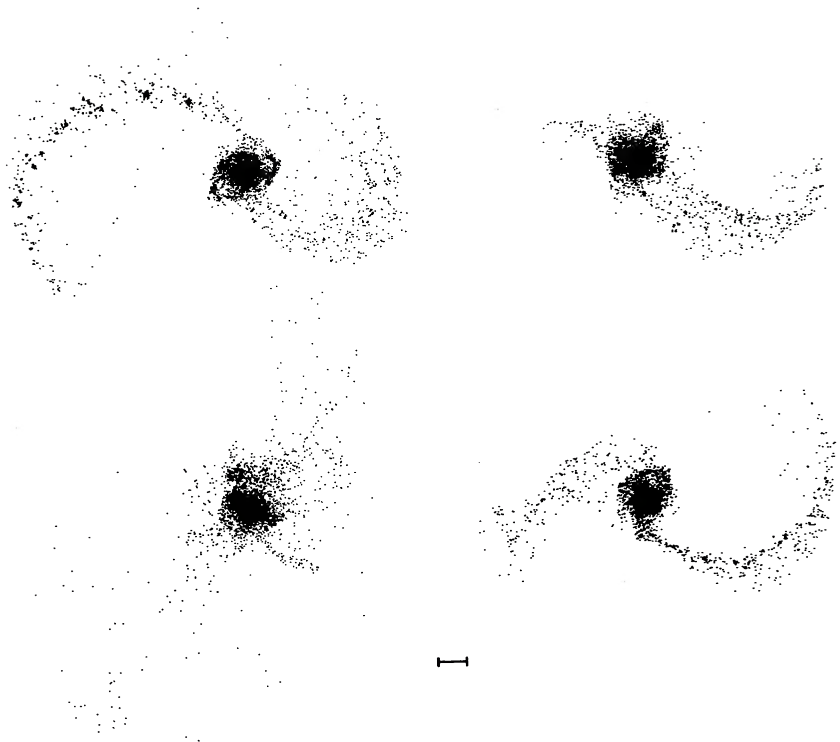

FIG. 12.—(*Clockwise from upper left*) Encounters 1, 2, 3, and 4 at time $t = 6$, projected onto the orbital plane. Each frame is 18 × 12 length units. For consistency with Fig. 2, encounter 4 has been rotated by 180°.

produced by the parabolic encounter of two "standard" galaxies, this argument predicts $\sigma_m^2 = 0.73$ and $r_g = 1.16$. Actual values of these parameters for remnant **B**, averaged between $t = 9$ and 10, are listed on the first line of Table 3; although

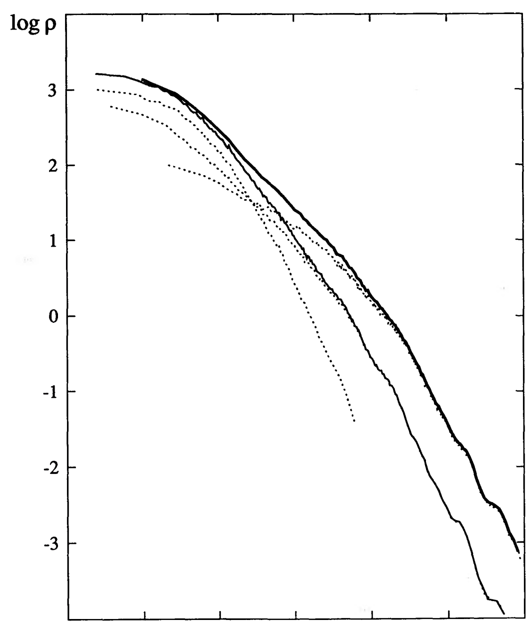

FIG. 13.—Spherically averaged density profiles for the merger remnant produced in encounter **B**. Heavy solid line shows total density, light solid line shows density in luminous (bulge + disk) material, and dotted lines show, in order of increasing central density, profiles for the halo, disk, and bulge populations, respectively.

escaping material and nonequilibrium effects modify the actual σ_m and r_g, the measured values are reasonably close to the predictions.

Following in Table 3 are similar measurements for various additional components of the merger remnant and an initial galaxy model. Also tabulated are virial ratios $-2T/U$. Here only gravitational interactions *within* a given component have been included when calculating U; thus $-2T/U > 1$ means that a component is bound in part by other components, not that it is out of equilibrium. With this convention, the "gravitational radii" r_g are essentially twice the harmonic-mean distance, $1/\langle 1/r_{ij} \rangle$, averaged over all pairs of particles in each component.

Comparing initial and final parameters in Table 3, it becomes clear that *only* for the total mass does the above conservation argument correctly predict the characteristic scale of the remnant (e.g., Farouki & Shapiro 1982; B88). As a result of merging, the velocity dispersions of the luminous

TABLE 3

PARAMETERS FOR REMNANT **B** AND AN INITIAL BULGE/DISK/HALO GALAXY

Component	M	σ_m^2	r_g	$-2T/U$
Remnant mass	2.382	0.73 ± 0.02	1.04 ± 0.02	0.96
Remnant light	0.495	0.79 ± 0.02	0.34 ± 0.01	1.6
Remnant bulge	0.125	0.66 ± 0.01	0.122 ± 0.002	1.9
Initial mass	1.25	0.73 ± 0.02	0.58 ± 0.02	0.98
Initial light	0.25	0.60 ± 0.02	0.240 ± 0.004	1.7
Initial bulge	0.0625	0.32 ± 0.02	0.088 ± 0.002	1.4

NOTE.—Bound masses, velocity dispersions, gravitational radii, and virial ratios for various components of the encounter **B** remnant and an initial bulge/disk/halo galaxy.

material in general and the bulge in particular increase by $\sim 15\%$ and $\sim 40\%$, respectively; moreover, the characteristic radii of these components increase by factors of only ~ 1.4 instead of 2 as expected. The conservation argument evidently fails because the final merger of the luminous components occurs from an orbit considerably more bound than the initial parabola. However, it is not easy to test this explanation quantitatively, since the luminous material is not gravitationally self-bound but evolved in conjunction with the halo material. Moreover, the final velocity dispersion of the bulge component is probably augmented by the incorporation of disk material during the merging process.

Before moving on to consider the shapes and rotation of merger remnants, it is of some interest to ask how these objects appear in projection. Figure 14 plots circularly averaged projected luminosity profiles for remnant **B** and for an initial disk galaxy. In Figure 14*a*, magnitude $\equiv -2.5$ log (surface brightness) is plotted against $r^{1/4}$, while in Figure 14*b* the independent variable is the projected radius r. Here as in many other studies of merging (e.g., White 1978; B88) and dynamical collapse (e.g., van Albada 1982; McGlynn 1984), violent relaxation establishes something close to a de Vaucouleurs law profile. The effective radius for this remnant, defined either by fitting a straight line to the curves in Figure 14*a* or by measuring the projected half-light radius, is $r_e \simeq 0.1$; other remnants in the present ensemble yield very similar results.

Of course, within $r \lesssim 0.3$ the *initial* face-on luminosity profile is not so different from an $r^{1/4}$ law, and at first sight merging appears to have done little more than smooth out the "shoulder" in the dotted profile which marks the transition between the bulge and the disk. In fact, much more radial redistribution has taken place; as noted above, a significant amount of disk material has been mixed in with the bulge at small radii. Consequently, the central surface brightness is reduced by only ~ 1 mag on setting the bulge luminosity to zero, and the disk material *alone* exhibits the beginnings of an $r^{1/4}$ profile, although with considerable curvature and a shallower slope than the total luminosity profiles plotted in Figure 14*a*. These results suggest that even pure exponential disks may be scrambled to produce de Vaucouleurs law profiles, although phase-space constraints may impose rather large core radii on the resulting remnants.

4.2. *Shapes and Kinematics*

Like several of the merger remnants described by Gerhard (1983a, b), the relic of encounter **A** shown in the lower frames of Figure 11 is prolate at small radii and becomes increasingly oblate farther out. Since these N-body models are still too grainy to permit the construction of smooth three-dimensional isopleths out to any appreciable radius, it is not clear how best to characterize remnant shapes. Gerhard divided merger remnants into shells, each of which contained a third of the mass, and estimated ellipticities separately for each shell; the use of spherical radii to define these shells introduced a bias which was calibrated by Monte Carlo tests. In the analysis presented here, particles will be binned by binding energy instead of radius. As Figure 15 shows, this tactic defines particle subsets which closely follow the overall shape of the system. The shape of each subset will be evaluated directly from the moment-of-inertia tensor,

$$\boldsymbol{I} \equiv \sum_i m_i \boldsymbol{x}_i \otimes \boldsymbol{x}_i , \tag{1}$$

where $\boldsymbol{x}_i$ is the position of particle i in a coordinate system accurately centered on the bottom of the potential well. No Monte Carlo tests have been done to calibrate the technique used here, but the results obtained are in good agreement with visual impressions and seem to be less biased than uncalibrated estimates obtained from subsets defined by spherical radius or potential energy. Shapes will be quoted in terms of the axial ratios of a homogeneous ellipsoid with the same moment of inertia; if $\boldsymbol{I}$ has eigenvalues $q_1 \geq q_2 \geq q_3$, then these ratios are $b \equiv (q_2/q_1)^{1/2}$ and $c \equiv (q_3/q_1)^{1/2}$. Principal axes will be defined by diagonalizing either $\boldsymbol{I}$ or the "normalized" tensor,

$$\boldsymbol{D} \equiv \sum_i m_i \frac{\boldsymbol{x}_i \otimes \boldsymbol{x}_i}{|\boldsymbol{x}_i|^2} , \tag{2}$$

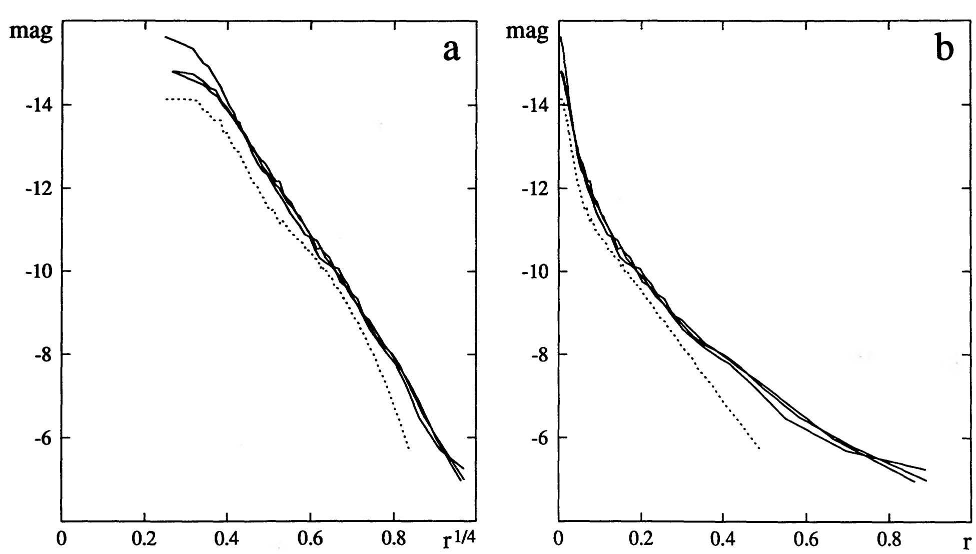

FIG. 14.—Projected luminosity densities plotted (*a*) against $r^{1/4}$ and (*b*) against r. The solid curves are the remnant from encounter **B**, projected along its three principal axes; the dotted curve is an initial disk galaxy, projected along the disk axis.

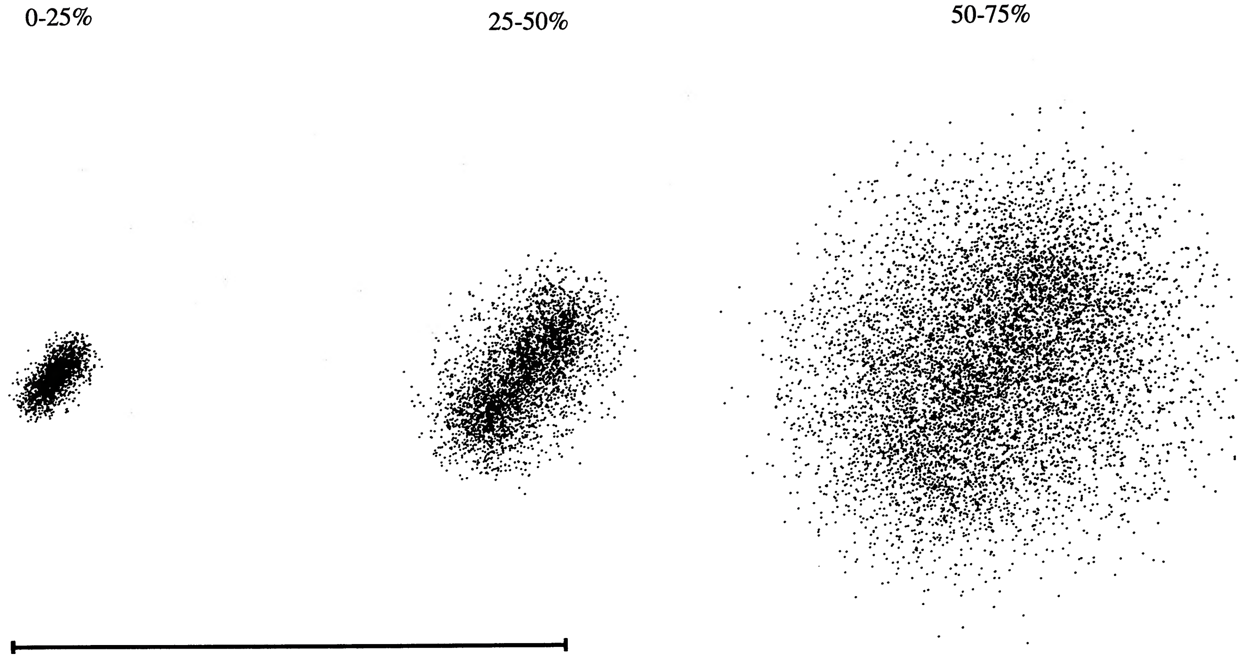

FIG. 15.—Luminous particles from the remnant produced by encounter **A** at time $t = 6$, binned by their specific binding energy. On the left is the 0%–25% bin, thinned by a factor of 4 to reduce crowding. In the middle is the 25%–50% bin, thinned by a factor of 2. On the right is the 50%–75% bin.

used by Gerhard, which is less sensitve to outlying particles. In these calculations $\boldsymbol{I}$ and $\boldsymbol{D}$ typically yield principal axes aligned to within $\sim 5°$ or less, demonstrating that particles on the outskirts do not dominate the moment of inertia.

In general, the principal axes of these remnants are not stationary but evolve with time. Figure 16 presents perspective views showing the evolution of the principal axes of remnants **A** and **B**. Results are plotted for the three binding energy bins shown in Figure 15; the small insets in Figure 16*a* show principal axes for the 75%–87.5% bin. The most tightly bound 75% of the luminous particles in remnant **A** form a prolate bar rotating about its minor axis with a pattern speed of ~ 0.3 radians per time unit. The 75%–87.5% bin, on the other hand, seems not to participate in this figure rotation but remains approximately fixed in space, with its major axis always roughly parallel to the x-direction and its minor axis tipped by $\sim 25°$ from the z-direction. The tilt is a residue of the original 71° tilt of one of the two disks involved in this merger. While this object has not been tracked beyond $t = 7$, its present structure does not seem to be violently unstable. Remnant **B**, on the other hand, is a more complicated case. Although major axes for the three most tightly bound quartiles of this remnant remain in rough alignment over the time interval shown, the other two axes exhibit large, rapidly evolving intrinsic twists. Between $t = 8$ and 10, the major axes swing through an angle of nearly 90°. Views at intermediate times suggest that the inner quartile of this remnant is also rotating about an axis instantly *parallel* to the major axis, with a pattern speed of ~ 1.2 radians per time unit.

The two remnants shown in Figure 16 are somewhat extreme examples. By way of comparison, the first eight numbered encounters in Table 1 produced three or four remnants with reasonably well-aligned axes or small intrinsic twists, two or three with larger intrinsic twists, and two nearly as scrambled as remnant **B**. In general, the rounder objects seem more prone to intrinsic twisting, possibly because the torques tending to reduce such twists are smaller in these systems. The large intrinsic twists and relatively rapid figure rotation of the most extreme of these objects may imply that they have not yet settled down to stable equilibria, although particles in the most tightly bound quartile of each remnant have had several dozen orbital periods of phase mixing since merger.

With this disclaimer issued, Figure 17 presents axial ratios for the three most tightly bound quartiles of the luminous particles in remnants **A**, **B**, and 1–8. These ratios were measured at least 2 time units after each merger was consummated, at $t = 6$ for the $R_p = 0.2$ encounters, and at $t = 8$ for their $R_p = 0.4$ counterparts. Also plotted are contours of constant triaxiality $\mathscr{T} \equiv (1 - b^2)/(1 - c^2)$, which ranges from $\mathscr{T} = 0$ for oblate spheroids to $\mathscr{T} = 1$ for prolate ones (e.g., de Zeeuw & Franx 1991). Many of the remnants produced in these experiments exhibit the same general trend of decreasing $\mathscr{T}$ with increasing radius noted by Gerhard (1983a, b), perhaps because stars flung out in the earlier stages of the encounter tend to be distributed toward the orbital plane, while those which hang on to the very end wind up in an elongated central structure formed by a nearly head-on collision. Nonetheless, the actual shapes of these remnants show considerable dependence on the initial orbit and inclinations of the victim disks. Wider collisions favour somewhat more oblate shapes, while inclined encounters generally produce rounder remnants (e.g., Farouki & Shapiro 1982; Negroponte & White 1983).

How much of a role does angular momentum play in shaping these merger remnants? The angular momentum content of a self-gravitating system is often expressed in terms of the dimensionless "spin parameter" $\lambda \equiv J/(G^2|E|^{-1}M^5)^{1/2}$; for example, a cold exponential disk all by itself has $\lambda \simeq 0.426$. As defined, however, λ cannot be used to quantify the angular

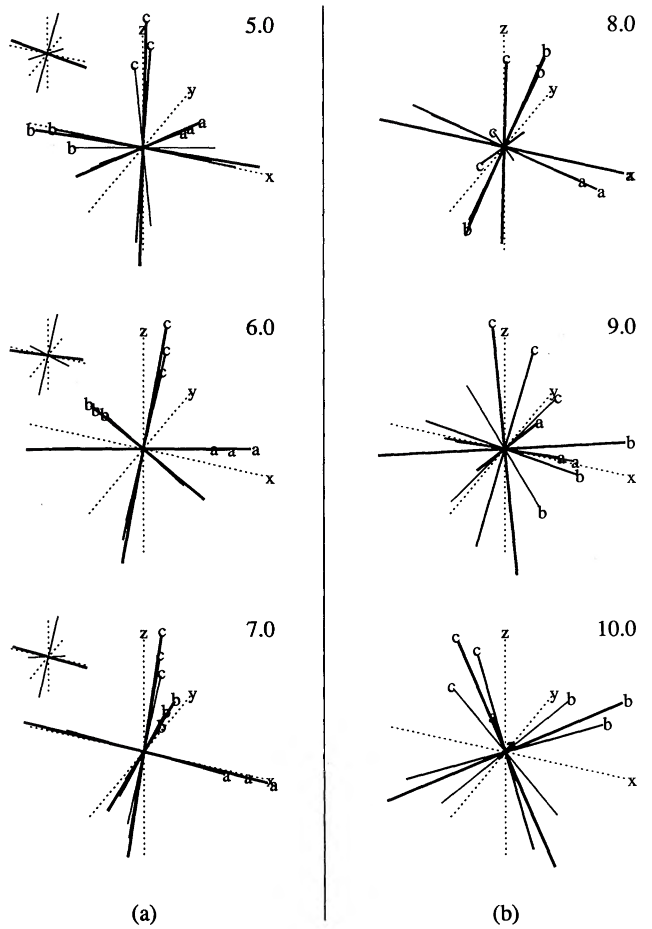

FIG. 16.—Perspective views showing the time evolution of the principal axes of the remnants produced by (*a*) encounter **A** and (*b*) encounter **B**. Elapsed time since the start of the simulation is shown in the upper right-hand corner of each frame. In both sets of plots, the shortest, lightest lines refer to the 0%–25% bin, the intermediate lines refer to the 25%–50% bin, and the longest, heaviest lines refer to the 50%–75% bin. For encounter **A** the small insets show the principal axes of the 75%–87.5% bin, with the major axis for this bin indicated by the heaviest line.

momentum content of a subset or component which is not entirely self-bound. Therefore, a new parameter,

$$\lambda' \equiv \frac{J}{J_{\max}}, \quad J_{\max} \equiv \sum_i m_i |\boldsymbol{x}_i| |\boldsymbol{v}_i| , \qquad (3)$$

will be used instead in this analysis. This parameter takes a maximal value $\lambda' = 1$ for a cold disk, regardless of whether it is self-bound or merely a test distribution.

Figure 18 plots the dimensionless spin parameter λ' against a characteristic ellipticity $\varepsilon \equiv 1 - (bc)^{1/2}$ for the same luminous subsets shown in Figure 17. Since λ' is a measure of intrinsic angular momentum while the quantity v/σ introduced by Binney (1978) is defined in terms of the rotational kinetic energy, this diagram cannot be interpreted as simply as the plots of v/σ against ε used to assess the rotational flattening of spheroids and elliptical galaxies (e.g., Davies et al. 1983). It is clear, however, that few of these remnants have significant rotational support; if anything, ellipticity and rotation are *anti*-correlated in this sample, with the most tightly bound bin showing the greatest flattening and the most loosely bound bin yielding the largest spin parameters. The relatively small λ' values and lack of positive correlation with ε suggest that, when plotted on a standard v/σ-ε diagram, most of these remnants would scatter well below the line expected for oblate isotropic rotators.

Given the triaxial shapes of these remnants and their rather modest degree of rotational support, one may anticipate that what angular momentum they do have may not be well aligned with their minor axes. In a stationary triaxial system the angular momentum vector may lie anywhere in the plane defined by the major and minor axes (e.g., Levison 1987; de Zeeuw & Franx 1991). Figure 19 plots ψ_c, the angle between the spin and the minor axis, against ψ_a, the angle between the spin and the major axis. While several remnants, notably those produced by the direct encounters 1 and 5, have spin vectors well aligned with their minor axes, others indeed exhibit large misalignments. This is perhaps most strikingly demonstrated by the 25%–50% bin, for which most of the spin vectors lie within 15° of the plane containing the major and minor axes. Similar misalignments are seen in the most tightly bound bin for remnants 2 and 3, but in remnants 6 and **B** the spin vectors have a significant component along the *intermediate* axis. This

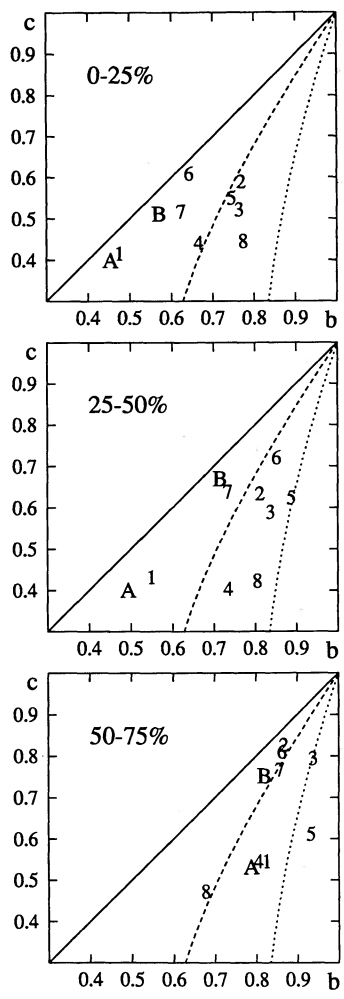

FIG. 17.—Axial ratios for the remnants produced by encounters **A**, **B**, and 1–8. Results are shown separately for the 0%–25% bin, the 25%–50% bin, and the 50%–75% bin. The solid, dashed, and dotted lines are contours of triaxiality $\mathscr{T} = 1, \frac{2}{3}$, and $\frac{1}{3}$, respectively.

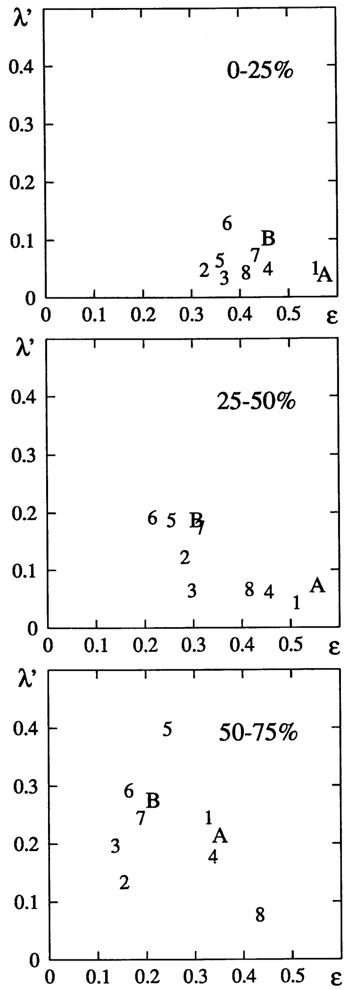

FIG. 18.—Dimensionless spin parameter λ' plotted against ellipticity ε. The symbols and layout are as in Fig. 17.

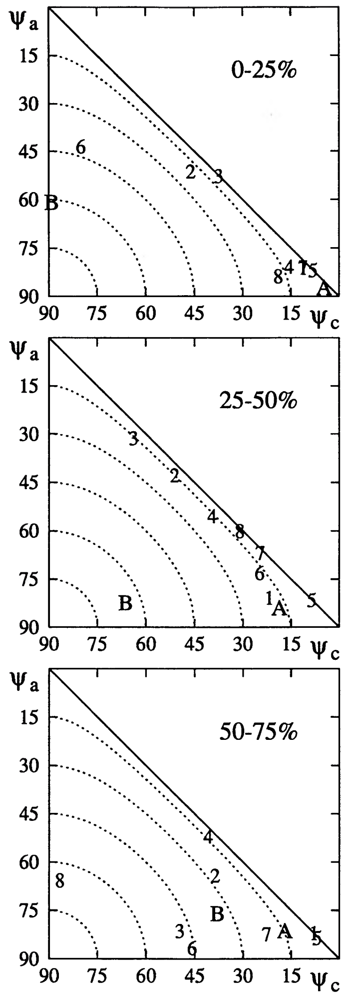

FIG. 19.—Misalignment angles ψ_c and ψ_a for the remnants produced by encounters 1–8. Symbols and layout are as in Fig. 17. Dotted lines are contours of constant ψ_b, the angle between the spin and intermediate-axis vectors.

may be related to the relatively rapid figure rotation of remnant **B** mentioned above. On the other hand, the large misalignments found in the most loosely bound bin may simply reflect incomplete phase mixing.

Before moving on to the orbit structure of these remnants, it is worth comparing the two $N = 65{,}536$ runs, encounters **A** and **B**, with their $N = 32{,}768$ analogs, encounters 1 and 6. As the last three figures show, remnants 1 and **A** are very similar in overall shape, angular momentum content, and lack of misalignment; such an outcome is hardly surprising in view of the rather robust structures of these remnants. The other two examples, remnants 6 and **B**, do not agree quite so well; at the precise instant ($t = 8$) when these properties were measured, the latter model is appreciably flatter throughout, and exhibits a dramatic misalignment in the 25%–50% bin. These discrepancies seem to trace back to rather small perturbations in the orbital trajectories of the two galaxies making up each remnant (§ 3.2). Thus, remnants 6 and **B** may both be characterized as rapidly tumbling spheroids with near-prolate shapes, differing largely in certain particulars which seem to depend sensitively on the arbitrarily chosen intitial orbit and the subsequent effects of $N^{1/2}$ fluctuations. In this respect these two clones are probably among the most sensitive and unstable of all the remnants described here.

4.3. *Orbit Structure*

Merger remnants generally assume triaxial figures which they can maintain for many crossing times after formation. The simplest generic triaxial models support box orbits, minor-axis tube orbits, and major-axis tube orbits (e.g., Schwarzschild 1979). Each of these orbital families is associated with a closed, stable orbit which determines the general shape of every orbit in the family. Thus all boxes may be thought of as perturbed versions of the stable orbit which shuttles back and forth along the major axis of a triaxial system. Likewise, minor-axis tubes derive from the closed orbit which loops around the minor axis of an oblate or triaxial configuration. Finally, *two* stable, topologically distinct orbits which loop about the major axis exist in many prolate or triaxial systems (e.g., de Zeeuw 1985); these parent two subfamilies of major-axis tubes. In an equilibrium configuration, particles must be distributed among the various orbital families so as to self-consistently generate the gravitational potential of the system. Equilibria constructed in this manner have been discussed by Schwarzschild (1979), Richstone (1984), and Statler (1987), among others.

This section is concerned with the inverse problem of "dissecting" triaxial, near-equilibrium N-body systems into their constituent orbital families. The general approach taken here is similar to that used by Sparke & Sellwood (1987) in dissecting rapidly rotating two-dimensional stellar bars; the present analysis extends their approach to three dimensions, but neglects figure rotation. Rotating triaxial systems have a very rich orbital structure (e.g., Martinet & de Zeeuw 1988); a full treatment including figure rotation is beyond the scope of this article. However, most of the merger remnants produced in this study show relatively slow figure rotation, so the present analysis should yield a reasonable first approximation to their true structure.

The first step was to set up a coordinate system (X, Y, Z) centered on the bottom of the remnant's potential well and aligned with its major, intermediate, and minor axes, respectively. This was done by calculating the center of mass and principal components of the inertia tensor for all particles within the equipotential surface $\phi < -8$, where $\phi(r = 0) \simeq -12$ and $\phi \to 0$ as $r \to \infty$. (As noted above, several remnants have large intrinsic twists, but this procedure gave acceptable results in most cases.) Next, the gravitational potential was expanded in Cartesian moments (e.g., White 1983b; Hernquist & Barnes 1990), truncated at quadrupole order. The field coefficients were tabulated on a 258 point radial grid, equally spaced in enclosed mass; linear interpolation was used to obtain the force at intermediate positions. For the rather spheroidal remnants studies here, forces calculated in this way agree to within $\sim 1\%$ with those computed using a tree; the main advantage of the expansion is the speed with which forces can be evaluated.

Individual particle orbits were followed with a time-centered leapfrog integrator, using time steps chosen to conserve energy to $\sim 0.1\%$. Each orbit was run for at least 30 radial periods to obtain a "fair sample" of its long-term behavior. At each time step the components of the instantaneous angular momentum vector $\boldsymbol{j} = (j_X, j_Y, j_Z)$ were compared with their values from the previous step, and sign changes were counted. Define k_I to be 1 if j_I does *not* change sign over the entire orbit, and 0 if it does, where the subscript I is one of X, Y, or Z. Then the quantity $k \equiv k_X + 2k_Y + 4k_Z$, which can take on values between 0 and 7, gives a crude classification of the orbit. A few loosely bound orbits could not be accurately integrated with a reasonable time step; these were flagged by $k = -1$. This procedure assigns a different k-value to each of the general orbit shapes expected in a generic triaxial potential. Orbits assigned $k = 0$ include the classical boxes as well as the various boxlets described by Miralda-Escudé & Schwarzschild (1989). Minor-axis (Z) tubes are assigned $k = 4$ and major-axis (X) tubes $k = 1$; this simple classification procedure cannot distinguish between the two subfamilies of X-tube orbits. Other k-values can occur, but such "deviants" are quite rare ($\lesssim 1\%$) among the most tightly bound 75% of the luminous particles. Note that stochastic orbits are not recognized as such by this procedure; some are classified as boxes, while others may retain a definite sense of circulation long enough to be classified as tubes.

Remnant 5, produced by a wide ($R_p = 0.4$) direct encounter, has a rather simple structure which is nicely elucidated by orbit analysis. As the results from the previous section indicate, this remnant has a relatively oblate form and a considerable amount of angular momentum, aligned almost exactly with the minor axis. Figure 20*a* shows the cumulative distribution of each orbital class k as a function of binding energy E. The procedure used to construct this diagram is as follows. First, the orbit classification procedure was applied to a blindly selected 1-in-4 sample of the luminous particles from remnant 5. Next, a total of nine solid curves were plotted, showing the cumulative distribution of orbits with $k \leq K$, where $K = -1$, 0, 1, ..., 7; all these curves were normalized by the number of particles in the sample. The first of these curves, plotted for $K = -1$, shows the cumulative fraction of unclassifiable orbits; since only a few such orbits occur, this curve is almost indistinguishable from the horizontal axis. The curves for $K = 0$, 1, and 4 are the *upper* envelopes for the regions representing box, X-tube, and Z-tube orbits, respectively. Thus, for example, at $E = -4$ the difference between the $K = 0$ and $K = 1$ curves indicates the fraction of luminous particles with

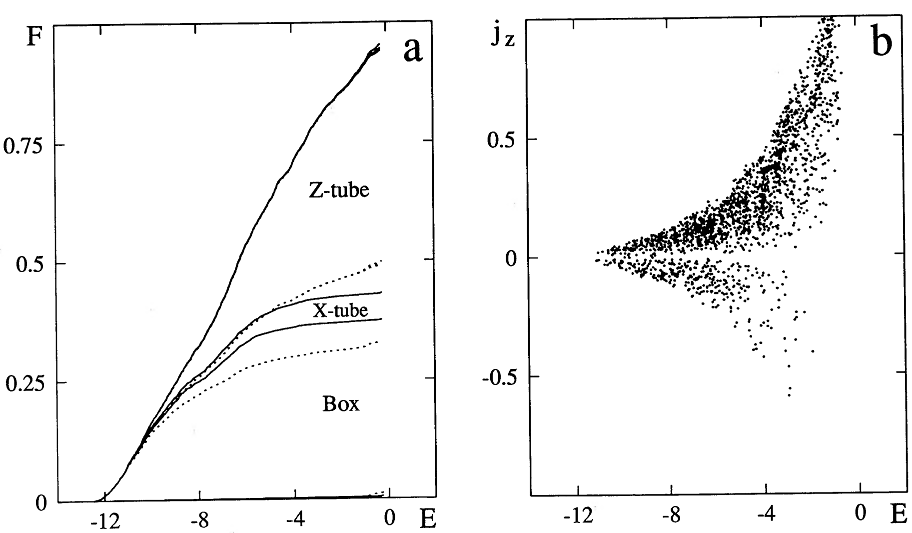

FIG. 20.—(*a*) Cumulative distribution of orbit class k for luminous particles from remnant 5, plotted as a function of binding energy E. (*b*) Z-component of angular momentum, j_Z, plotted against binding energy for the Z-tube orbits.

binding energies $E \leq -4$ on X-tube orbits. The most tightly bound particles in remnant 5 are almost all on box orbits, helping to support the triaxial shape of the central region. Farther out, the remnant is dominated by Z-tube orbits. In Figure 20*b* the angular momentum of the Z-tube orbits is plotted against their binding energy; as this figure shows, the vast majority of these tubes orbit the remnant in the same direction, accounting for the high λ' value of this object. Unlike most of the others in this study, remnant 5 appears to be largely flattened by rotation at larger radii. The rotation of this remnant is evidently a relic of the relatively high angular momentum of the initial orbit and the direct spins of the two disks involved.

The dotted lines in Figure 20*a* show the result of applying the orbit classification procedure to a isotropic test distribution with the same $f(E)$ as the luminous sample. This exercise measures the phase-space volume available to each orbital family in the system. The test distribution was constructed from the luminous sample by iterating the following pair of operations: (1) randomize the direction of the velocity vector of each particle, leaving the magnitude unchanged; (2) follow the new trajectory of each particle for a random period comparable to a few orbits. These operations leave $f(E)$ unchanged but erase any other structure the distribution may have. After five iterations the distribution converges on a unique limit as judged from the results of orbit classification. The available phase-space volume in the potential of remnant 5 is dominated by the box and Z-tube families. X-tube orbits are roughly half as common in the actual remnant as they are in the isotropic sample, a pattern common to many of the remnants studied here.

A very different result ensues from encounter 8, the retrograde analog of the one just described. The resulting remnant, with an axial ratio $c \lesssim 0.5$, is one of the few in this study which becomes more prolate at larger radii; it is unique in having $\lambda' < 0.1$ even in the 50%–75% energy bin. As Figure 21*a* shows, remnant 8 has a significantly larger population of box orbits than remnant 5. It is also strikingly deficient in X-tube orbits, both absolutely and relative to the available phase-space volume. In Figure 21*b* open circles refer to orbits of particles in the luminous component, while points refer to those in the dark halo. The distribution of Z-tube orbits more tightly bound than $E = -4$ is almost symmetric with respect to $j_Z = 0$, in accord with the low λ' value quoted above. For orbits with $E > -4$, the luminous and dark components stream in opposite directions; the halo has become the repository for the orbital angular momentum of the two initial galaxies, while the streaming of the luminous material reflects the retrograde spins of the disks. The spatial distribution of the luminous particles on Z-tube orbits with $j_Z < 0$ and binding energies $-4 < E < -2$ is noteworthy; these form a thick disk, inclined at an angle of $\sim 25°$ with respect to the X-Y plane. In time, differential precession should "wind up" this disk, possibly producing an object with box-shaped isophotes at large radii.

Figure 22 presents the orbital structure of remnant 2, produced by a relatively close ($R_p = 0.2$) encounter between two inclined disks. This object is somewhat rounder than the two remnants just described; moreover, as Figure 19 shows, it exhibits a significant intrinsic misalignment between spin and minor axis. The cumulative distribution of orbital families is shown in Figure 22*a*. A relatively large fraction of the luminous particles are on X-tube orbits, although this family is still underpopulated with respect to the phase space available. Figure 22*b* plots the angular momentum of these X-tube orbits against binding energy; circles are particles from galaxy 1, crosses from galaxy 2. Orbits more tightly bound than $E = -6$ are distinctly asymmetric with respect to $j_X = 0$, giving the inner half of this remnant a significant component of angular momentum along its major axis. For $E > -6$ this overall j_X distribution is somewhat more symmetric; note, however, that particles from galaxy 1 tend to have $j_X > 0$, while those from the other galaxy tend to have the opposite sign. The counter-streaming of these two subpopulations reflects the antiparallel spin vectors of the initial disks.

The three examples just presented do not exhaust the range of orbit structure found in this set of merger remnants. Mergers in which both disks are inclined generally yield more X-tube orbits than those in which one disk is either direct or retrograde, while wider encounters favor Z-tube orbits. Besides

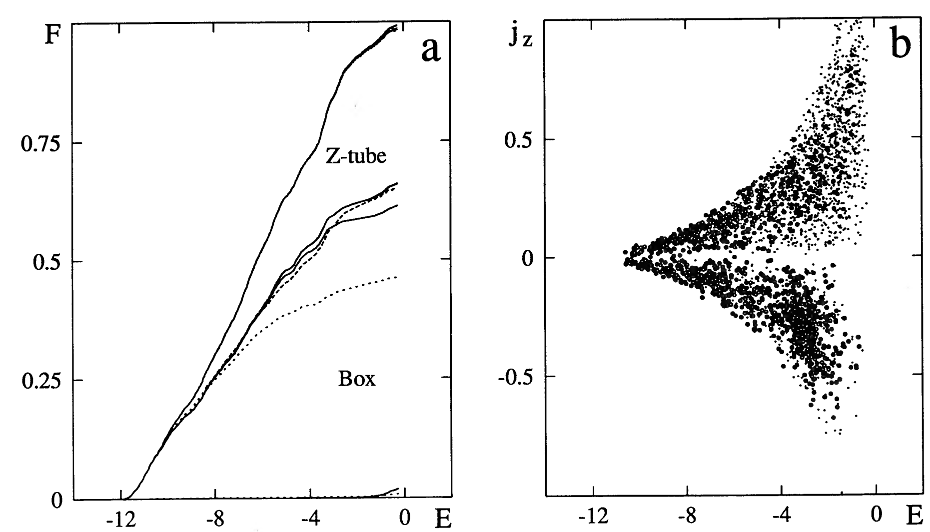

FIG. 21.—(*a*) Cumulative distribution of orbit class *k* for luminous particles from remnant 8, plotted as a function of binding energy *E*. (*b*) Z-component of angular momentum, j_Z, plotted against binding energy for the Z-tube orbits. Points refer to halo particles, circles to luminous particles.

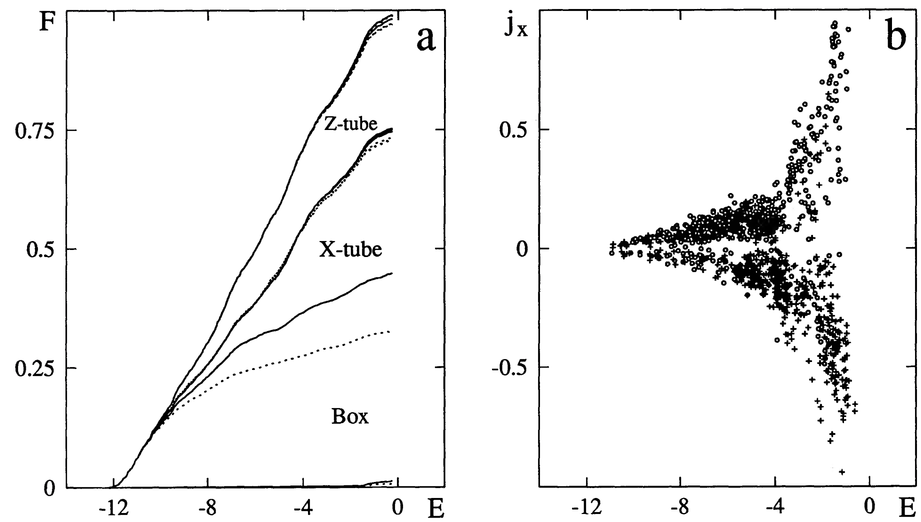

FIG. 22.—(*a*) Cumulative distribution of orbit class k for luminous particles from remnant 2, plotted as a function of binding energy E. (*b*) X-component of angular momentum, j_X, plotted against binding energy for the X-tube orbits. Circles are particles from galaxy 1, crosses from galaxy 2.

remnant 2, several others, including remnants 3, 4, and 8, have X-tube populations asymmetrically distributed with respect to $j_X = 0$ and consequently exhibit appreciable spin misalignment. Other remnants, such as **A**, exhibit curious substructures in plots of angular momentum versus binding energy. Finally, the simple analysis of orbit structure presented here fails for remnants 6 and **B**; these objects, which have strongly twisted axes and rapid figure rotation, yield significant numbers of deviant orbits ($k \neq 0$, 1, or 4). Longer self-consistent calculations are required to determine whether such remnants are quasi-stable in the sense discussed by Gerhard (1983a).

It seems likely that some remnants, particularly those with rapid figure rotation, contain particles on stochastic orbits. Such orbits can be difficult to identify in self-consistent models, since potential fluctuations due to particle discreteness can scatter otherwise regular trajectories; depending on the treatment of the potential, the stochastic fraction may be as much as 100% if orbits are followed for sufficiently long times. Only violently stochastic orbits are likely to drastically modify the structure of merger remnants, however, and the stochastic character of such orbits may turn out to be reasonably robust with respect to small perturbations in the potential. Further work on this problem could prove quite interesting, since merging may create objects with significant populations of stochastic orbits.

5. DISCUSSION

Before summarizing the results of these calculations, it seems appropriate to mention some limitations and drawbacks. Within the context of purely collisionless calculations, the N-body code does an acceptable job; further improvements, such as individual particle time steps, may make the code more efficient but probably not significantly more accurate. The initial conditions, on the other hand, can be much improved.

First, the bulge/disk/halo galaxy models used for these runs are not as centrally concentrated as real galaxies; the initial bulges have core radii of ~ 0.02 length units (just under 1 kpc, adopting the scaling in § 2.1), and central densities only ~ 50 times the mean density within the half-mass radius. As already noted, these flabby cores present excessively easy targets during the last passages and inflate the final core radii of merger remnants. More concentrated spheroidal components would also give the initial disks more steeply rising rotation curves, a modification which might reduce the incidence of tidally induced bars in these calculations. To create and run models with significantly more concentrated cores requires calculations with smaller values for the softening parameter ϵ. Such changes are relatively straightforward but may prove computationally expensive.

Second, the properties of the initial spheroids are rather artificial. Bulges and halos are both built from low-concentration King (1966) models, lacking initial rotation or velocity anisotropies. It seems quite likely that these attributes could affect the outcome of merger calculations; halo rotation would change the time scale of orbital decay, while bulge rotation might influence the angular momentum content of the central regions of merger remnants. While there are relatively easy ways to impart rotation or velocity anisotropy to spheroidal systems (e.g., Barnes & White 1984), these ad hoc tricks are poor substitutes for properly specified models whose detailed properties can be predicted without resorting to N-body calculations. Further work on the construction of oblate equilibrium systems is required to address this problem.

Third, several "shortcuts" were used in these runs. For example, identical spheroid realizations were employed in distinct calculations, although disk particles were laid down independently each time. This explains why, in Figure 8, encounters 9 and 10 show such similar wiggles before first passage. While this saved considerable time in generating initial conditions and probably has no great influence on the outcome of the calculations, it is clearly less rigorous than one might desire. Another shortcut, sanctioned by previous use (B88) but not properly tested, is the 4:1 mass ratio between dark and lumimous particles; if the halo really is the leading source of noise in these calculations, a smaller ratio might have proved more effective, even at the expense of reducing the number of disk particles run. Moreover, the calculations were started with the two galaxies relatively close together in order to reduce the effects of disk heating and save computer time; this may somewhat perturb the equilibria of the initial halos.

Fourth and finally, fluctuations due to the discreteness of the N-body representation severely limit the accuracy of these calculations. As van Albada (1987) showed, such fluctuations perturb the integrals of motion of individual particles in equilibrium systems, driving what amounts to a diffusive process in action space. Hernquist & Barnes (1990) have argued that these fluctuations are *intrinsic* to N-body simulations; they cannot be suppressed by smoothing the force calculation without sacrificing spatial resolution. The only cure is to increase N.

These points serve as reminders that the present models, although more ambitious than previous efforts, are still only caricatures of real interacting galaxies. Faster computers and better techniques for generating initial conditions will render these models obsolete. But at the same time, the physical mechanisms illustrated in these calculations *are* among those occurring in real systems. For purposes of illustration, a caricature is acceptable, and sometimes even preferable.

When compared with those in B88, these models show what a wealth of detail has become visible with a mere quadrupling of N. The earlier calculations, while certainly yielding convincing tidal features, gave little feel for the internal evolution of interacting disk systems. The present models vividly illustrate the tidal forcing of grand-design spirals and bars, in accord with previous and generally more restricted calculations (e.g., Toomre 1981; Noguchi 1987; Hernquist 1990). The new calculations also illustrate the tidal origins of less well-known features, including the shell-like structures resulting from encounters with significant mass transfer and the short-lived ring morphologies produced in off-axis, but plunging, passages.

These calculations have also shed yet more light on the process of orbital decay in multicomponent systems. When two galaxies meet, it is always the most extended components which interact tidally, and the sense of this interaction is to transmute orbital angular momentum into internal rotation. The tightly bound components, on the other hand, suffer no direct interaction; only when the central regions of each galaxy begin pulling ahead of their accompanying halos do they begin to feel the effects of the encounter. As emphasized above, this means that the tightly bound material can lose its orbital angular momentum without acquiring internal rotation.

While violent relaxation partly redistributes binding energy between particles, and roughly doubles the total central spatial density in these experiments, maximum *phase-space* densities cannot increase, by Liouville's theorem. As in previous experiments (e.g., Melott 1982; Farouki, Shapiro, & Duncan 1983; May & van Albada 1984), pressure-supported components such as bulges merge with little decrease in the coarse-grained f_{max}. On the other hand, the coarse-grained phase-space density of the *disk* material shows a large drop during the merging process. This seems to go hand in hand with violence required to destroy the disks themselves.

Orbit classification (e.g, Wilkinson & de Zeeuw 1987; Sparke & Sellwood 1987) provides a powerful tool for analyzing the structure of merger remnants. In general, merging can populate the X-tube and Z-tube orbit families in a nonuniform manner, producing both major- and minor-axis rotation and consequent misalignments between the net angular momentum and minor axes. The different components of merger remnants frequently exhibit distinctly different kinematics. Thus, as prefigured in earlier studies (e.g., Gerhard 1983a, b), mergers between model disk galaxies produce remnants with complex internal structure. Merging leaves its mark, but the exact form depends on the geometry of the original encounter; there is not one merger signature, but many. Remnants span a wide range of ellipticity and triaxiality; they are flattened more by velocity anisotropy than by rotation. It is not clear whether these objects can maintain their shapes indefinitely, or whether they are subject to secular evolution on time scales longer than a few dynamical times; N-body models are probably to noisy to answer this question fully. However, recent analytic results on "writing spheroids" (Sridhar & Nityananda 1990) and N-body experiments producing systems tumbling about their intermediate axes (Duncan & Levison 1989) hint that the range of stable equilibria may indeed contain some surprises.

Several recent observational studies have found that the isophotes of elliptical galaxies depart from pure ellipses at the $\sim 1\%$ level (e.g., Bender 1990). These observations have led to the suggestion that elliptical galaxies come in two varieties: "boxy" ellipticals, which may be merger remnants of relatively recent vintage, and "disky" ellipticals, which presumably have some other origin. The former class of objects tend to be significantly brighter in both X-ray and radio continuum bands, while the latter are generally rapid rotators. While this "dichotomy hypothesis" (e.g., Nieto & Bender 1989) seems useful in organizing and interpreting the observational data, the theoretical justification is perhaps not as solid as one would like. For example, it is possible that merger remnants like the one produced by encounter 5 may mimic both the rapid rotation and the pointed isophotes of disky ellipticals. It would clearly be interesting to study the projected "isophote" shapes of the present merger remnants, but a careful analysis is required, since the number of particles in these models falls far short of the number of photons captured in a typical CCD frame.

The axial ratios, triaxialities, and misalignments found in this ensemble of merger remnants invite comparison with the extensive photometric and kinematic data compiled by Franx, Illingworth, & de Zeeuw (1991) to constrain the shapes of elliptical galaxies. From apparent ellipticities of a large sample of elliptical galaxies these authors obtain *intrinsic* ellipticity distributions with a broad peak at $c \simeq 0.6$–0.7; while the observed ellipticities do not fully constrain the three-dimensional shapes of the galaxies, model distributions containing only oblate systems yield a few too many round galaxies. The broad distribution of remnant ellipticities and triaxialities seen in Figure 17 seems quite consistent with the models constructed by Franx et al. Kinematic properties for a smaller sample of relatively round galaxies tell a somewhat different story. Franx et al. constructed several intrinsic misalignment and triaxiality distributions consistent with this sample and found in every case that at least 35% of the galaxies have intrinsic misalignments $\psi_c \lesssim 15°$. For all these solutions the mean triaxialities and misalignments are $\langle \mathscr{T} \rangle \leq 0.7$ and $\langle \psi_c \rangle \leq 45°$; however, only those solutions in which the actual distributions of $\mathscr{T}$ and ψ_c are bimodal allow such large mean values. Although the distribution of elliptical galaxies in the $\mathscr{T}$-ψ_c plane is severely underconstrained, the data suggest that a significant fraction are oblate or triaxial with small misalignments, while a smaller fraction are nearly prolate with $\psi_c \simeq 90°$. Figure 19 shows that roughly half of the remnants described here have intrinsic misalignments $\psi_c \lesssim 15°$ at small radii, but these objects have triaxialities $\mathscr{T} \gtrsim \frac{2}{3}$ and so would exhibit large apparent misalignments from most viewing angles. Farther out, most of these remnants have intrinsic misalignments distributed in the range $0 \lesssim \psi_c \lesssim 60°$. While it would be interesting to measure the apparent misalignments of these remnants by conducting simulated observations from a variety of viewing angles, it seems likely that the resulting distribution would be considerably flatter than the actual distribution of such misalignments plotted by Franx et al. in their Figure 17*a*.

If further experiments covering a wider range of encounter parameters and using more realistic galaxy models reproduce the rather large number of misaligned remnants found in this study, then it would appear that most elliptical galaxies were *not* formed by purely stellar-dynamical mergers of nearly equal-mass galaxies. In this case, several distinct interpretations may be given. One possibility is that most elliptical galaxies formed as a result of highly dissipative mergers between extremely gas-rich objects, and that most of the stars in these elliptical galaxies formed during or even after the merger proper (Ostriker 1980; Kormendy 1990). While this option cannot be excluded, it would seem beyond the reach of numerical modeling; without some fairly fundamental breakthrough in our understanding of star formation, we have no means to predict the detailed structure of the remnants produced by highly dissipative mergers. A second possibility, at the opposite extreme from the first, is that most elliptical galaxies were produced by multiple but purely stellar-dynamical collisions. It is quite likely that multiple mergers occur as a result of dynamical evolution in compact groups of galaxies (e.g., White 1990) and in other physical settings, but until more numerical models of such mergers become available, it will not be possible to say what fraction of the remnants show significant misalignments. A third possibility, perhaps the most intriguing, is that the rather modest amounts of gas present in mergers between typical disk galaxies may significantly perturb the dynamics of the stellar component. Such gas may collect at the center of the merger remnant, where its gravitational field could destabilize the box orbits which underpin the triaxial shapes of the remnants described here (Gerhard & Binney 1985; Norman, May, & van Albada 1985). Alternatively, it may settle into a nearly circular disk, thereby tending to favor a more axisymmetric structure (Franx et al. 1991); since such disks might on occasion align perpendicular to the major axis, this mechanism could naturally account for the small fraction of elliptical galaxies which seem to be major-axis rotators. It should be possible to study these effects with numerical models. Several of the encounters described here have now been rerun with a combined N-body/gasdynamical code (Barnes & Hernquist 1991; Hernquist & Barnes 1991), and we hope to present further results of this investigation in the near future.

Many people offered valuable comments and suggestions in the course of this work, but Marijn Franx, Lars Hernquist, François Schweizer, Jerry Sellwood, and Alar Toomre have made special contributions, and I take pleasure in thanking them. The hospitality and support of Scott Tremaine and the Canadian Institute for Theoretical Astrophysics, where much of the analysis was performed, is gratefully acknowledged. Numerical calculations were run at the John von Neumann and Pittsburg Supercomputing Centers under grants LAC-17016 and AST-910001P, respectively. Anjana Kar and Joel Welling of Pittsburgh Supercomputing Center provided invaluable assistance in creating the videotape.

APPENDIX A

BULGE/DISK/HALO GALAXY MODELS

As in B88, the procedure used to set up the spheroidal components in approximate dynamical equilibrium begins with the construction of N-body realizations of two separate King (1966) models which represent the bulge and halo. These two systems are superposed and allowed to relax for several halo dynamical times by following their evolution with a simple "spherical harmonic" N-body code (e.g., White 1983b). After they have relaxed, the gravitational field $\Phi_d(r, z)$ of an exponential disk is slowly imposed, adiabatically compressing the bulge and the halo as in the models of Barnes & White (1984) and Barnes (1987). At the end of this process, the bulge and halo have come into near-equilibrium in the presence of each other and the disk field. The circular orbital velocity in the disk plane, $v_c(r)$, is approximated by

$$v_c \simeq \left[r \frac{\partial \Phi_d}{\partial r} + \frac{GM_s(<r)}{r} \right]^{1/2} , \tag{A1}$$

where $M_s(<r)$ is the total bulge and halo mass within a sphere of radius r. Here the flattening of the spheroidal components has been ignored; however, the bulge and halo are very nearly round even in the presence of the disk field, so no significant error is introduced.

Next, the disk is realized with particles laid down according to the following distribution:

$$f_d(\mathbf{x}, \mathbf{v}) \propto e^{-\alpha r} \operatorname{sech}^2 \left(\frac{z}{z_0}\right) \exp\left(\frac{-v_r^2}{2\sigma_r^2}\right) \exp\left[\frac{-(v_\phi - v_d)^2}{2\sigma_\phi^2}\right] \exp\left(\frac{-v_z^2}{2\sigma_z^2}\right) . \tag{A2}$$

Here α^{-1} and z_0 are the radial and vertical disk scale lengths, respectively; the latter is taken to be independent of r, specifying a constant–scale-height disk (e.g., van der Kruit & Searle 1981). The vertical velocity dispersion $\sigma_z(r)$ is taken from the isothermal sheet model,

$$\sigma_z = (\pi G \Sigma_d z_0)^{1/2} , \tag{A3a}$$

where $\Sigma_d(r) = (M_d \alpha^2/2\pi)e^{-\alpha r}$ is the surface density of the disk. The radial velocity dispersion $\sigma_r(r)$ is fixed by assuming the following relation:

$$\sigma_r = \mu\sigma_z \, , \tag{A3b}$$

where the parameter μ is equal to 2 everywhere, comparable to the local ratio in the solar neighborhood. The tangential dispersion $\sigma_\phi(r)$ is given by epicyclic theory:

$$\sigma_\phi = \frac{\kappa}{2\omega}\sigma_r \, , \tag{A3c}$$

where $\omega(r) = v_c/r$ and $\kappa(r) = (4\omega^2 + r\, d\omega^2/dr)^{1/2}$ are the orbital and epicyclic frequencies, respectively. Finally, the mean circular velocity of the disk, $v_d(r)$, is obtained by inserting equations (A2) and (A3) into the Jeans equation in cylindrical coordinates (e.g., Binney & Tremaine 1987, § 4.2):

$$v_d = \left[v_c^2 - \sigma_r^2\left(2\alpha r + \frac{\kappa^2}{4\omega^2} - 1\right)\right]^{1/2} . \tag{A4}$$

In the innermost 2% or 3% of the disk, the approximations used to derive this equation break down and the argument to the square root may become negative; if so, $v_d = 0$ is used instead.

APPENDIX B

THE VIDEO SEQUENCES

The eight video sequences accompanying this paper (ApJ, 393, Part 1, No. 2, Videotape, Segment 2, sections 1–8) are all based on encounter A. A consistent coloring scheme is used throughout, with halo material shown in red, disk particles in blue, and the central bulges in yellow; intensity provides an indication of particle density. Listed in order, the video shows the following:

1. The initial conditions, rotated by 360° about the vertical axis. The incoming parabolic trajectories assigned to the two galaxies are shown in green.
2. Time evolution from $t = 0$ to $t = 4$, showing the initial approach, formation of tails, and merger.
3. The two galaxies at $t = 1.5$, rotated about the vertical.
4. Face-on view of the direct disk from $t = 0.5$ to $t = 2.0$; the location of the companion is shown as a white circle.
5. Face-on view of the inclined disk; other details are as for section 4 of the videotape segment.
6. Time evolution from $t = 2$ to $t = 6$, showing the second approach, merger, and relaxation of the remnant.
7. The merger remnant at $t = 3$, rotated about the vertical.
8. The merger remnant at $t = 6$, rotated about the vertical.

REFERENCES

Alladin, S. 1965, ApJ, 141, 768
Balcells, M., & Quinn, P. 1990, ApJ, 361, 381
Barnes, J. 1987, in Nearly Normal Galaxies, ed. S. Faber (New York: Springer-Verlag)
———. 1988, ApJ, 331, 699 (B88)
———. 1990a, in Dynamics and Interactions of Galaxies, ed. R. Wielen (Heidelberg: Springer-Verlag), 232
———. 1990b, J. Comput. Phys., 87, 161
Barnes, J., & Hernquist, L. 1991, ApJ, 370, L65
Barnes, J., & Hut, P. 1986, Nature, 324, 446
Barnes, J., & White, S. 1984, MNRAS, 211, 753
Bender, R. 1990, in Dynamics and Interactions of Galaxies, ed. R. Wielen (Heidelberg: Springer-Verlag), 232
Binney, J. 1978, MNRAS, 183, 501
Binney, J., & Petrou, M. 1985, MNRAS, 214, 449
Binney, J., & Tremaine, S. 1987, Galactic Dynamics (Princeton: Princeton Univ. Press)
Carlberg, R. 1987, in Structure and Dynamics of Elliptical Galaxies, ed. T. de Zeeuw (Dordrecht: Reidel), 353
Carlberg, R., & Sellwood, J. 1985, ApJ, 292, 79
Davies, R., Efstathiou, G., Fall, M., Illingworth, G., & Schechter, P. 1983, ApJ, 266, 41
de Zeeuw, T. 1985, MNRAS, 216, 273
de Zeeuw, T., & Franx, M. 1991, ARA&A, 29, 239
Duncan, M., & Levison, H, 1989, ApJ, 339, L17
Efstathiou, G. 1990, in Dynamics and Interactions of Galaxies, ed. R. Wielen (Heidelberg: Springer-Verlag), 2
Farouki, R., & Shapiro, S. 1982, ApJ, 259, 103
Farouki, R., Shapiro, S., & Duncan, M. 1983, ApJ, 265, 597
Franx, M., & Illingworth, G. 1990, ApJ, 359, L41
Franx, M., Illingworth, G., & de Zeeuw, T. 1991, ApJ, 383, 12
Gerhard, O. 1983a, MNRAS, 202, 1159
———. 1983b, MNRAS, 203, 19P
Gerhard, O., & Binney, J. 1985, MNRAS, 216, 467
Greengard, L. 1990, Comput. Physics, 4, 142
Hausman, M., & Ostriker, J. 1978, ApJ, 224, 320
Hernquist, L. 1987, ApJS, 64, 715
———. 1990, in Dynamics and Interactions of Galaxies, ed. R. Wielen (Heidelberg: Springer-Verlag), 108
Hernquist, L., & Barnes, J. 1990, ApJ, 349, 562
———. 1991, Nature, 354, 210
Holmberg, E. 1941, ApJ, 94, 385
Jaffe, W. 1987, in Structure and Dynamics of Elliptical Galaxies, ed. T. de Zeeuw (Dordrecht: Reidel), 511
King, I. 1966, AJ, 76, 64
Kormendy, J. 1984, ApJ, 287, 577
———. 1990, in Dynamics and Interactions of Galaxies, ed. R. Wielen (Heidelberg: Springer-Verlag), 499
Larson, R. 1974, MNRAS, 169, 229
Levison, H. 1987, ApJ, 320, L93
Lynden-Bell, D. 1987, MNRAS, 136, 101
Lynds, R., & Toomre, A. 1976, ApJ, 209, 382
Martinet, L., & de Zeeuw, T. 1988, A&A, 206, 269
May, A., & van Albada, T. 1984, MNRAS, 209, 15
McGlynn, T. 1984, ApJ, 281, 13
Melott, A. 1982, Phys. Rev. Lett., 48, 892
Miralda-Escudé, J., & Schwarzschild, M. 1989, ApJ, 339, 752
Negroponte, J., & White, S. 1983, MNRAS, 205, 1009
Nieto, J.-L., & Bender, R. 1989, A&A, 215, 266
Noguchi, M. 1987, MNRAS, 228, 635
Norman, C., May, A., & van Albada, T. 1985, ApJ, 296, 20
Ostriker, J. 1980, Comm. Astrophys., 8, 177
Palmer, P. L., & Papaloizou, J. 1982, MNRAS, 199, 869
Quinn, P. J. 1984, ApJ, 279, 596
Richstone, D. 1984, ApJ, 281, 100
Rood, H., Page, T. L., Kintner, E. C., & King, I. R. 1972, ApJ, 175, 627

Schwarzschild, M. 1979, ApJ, 232, 236
Schweizer, F. 1982, ApJ, 252, 455
———. 1990, in Dynamics and Interactions of Galaxies, ed. R. Wielen (Heidelberg: Springer-Verlag), 60
Sparke, L., & Sellwood, J. 1987, MNRAS, 225, 653
Sridhar, S., & Nityananda, R. 1990, in Dynamics and Interactions of Galaxies, ed. R. Wielen (Heidelberg: Springer-Verlag), 375
Statler, T. 1987, ApJ, 321, 113
Toomre, A. 1977, in The Evolution of Galaxies and Stellar Populations, ed. B. M. Tinsley & R. B. Larson (New Haven: Yale Univ. Observatory), 401
———. 1978, in The Large Scale Structure of the Universe, ed. M. S. Longair & J. Einasto (Dordrecht: Reidel), 109
———. 1981, in The Structure and Evolution of Normal Galaxies, ed. S. M. Fall & D. Lynden-Bell (Cambridge: Cambridge Univ. Press), 111
Toomre, A., & Toomre, J. 1972, ApJ, 179, 623 (TT)
van Albada, T. 1982, MNRAS, 201, 939
van Albada, T. 1987, in Structure and Dynamics of Elliptical Galaxies, ed. T. de Zeeuw (Dordrecht: Reidel), 291
van der Kruit, P., & Searle, L. 1981, A&A, 95, 105
White, S. 1978, MNRAS, 184, 185
———. 1979, MNRAS, 189, 831
———. 1983a, in Internal Kinematics and Dynamics of Galaxies, ed. E. Athanassoula (Dordrecht: Reidel), 337
———. 1983b, ApJ, 274, 53
———. 1987, in Structure and Dynamics of Elliptical Galaxies, ed. T. de Zeeuw (Dordrecht: Reidel), 339
———. 1990, in Dynamics and Interactions of Galaxies, ed. R. Wielen (Heidelberg: Springer-Verlag), 380
White S., & Rees, M. 1978, MNRAS, 183, 341
Wilkinson, A., & de Zeeuw, T. 1987, in Structure and Dynamics of Elliptical Galaxies, ed. T. de Zeeuw (Dordrecht: Reidel), 485